

NUREG/CR-6259
UILU-ENG-94-2009
ORNL/TM-12796

Constraint Effects on Fracture Initiation Loads in HSST Wide-Plate Tests

Manuscript Completed: August 1994
Date Published: December 1994

Prepared by
R. H. Dodds, Jr.

University of Illinois
Urbana, IL 61801

Under contract to:
Oak Ridge National Laboratory
Operated by Martin Marietta Energy Systems, Inc.

Oak Ridge National Laboratory
Oak Ridge, TN 37831-6285

Prepared for
Division of Engineering
Office of Nuclear Regulatory Research
U.S. Nuclear Regulatory Commission
Washington, DC 20555-0001
NRC Job Code B0119

MASTER

DISTRIBUTION OF THIS DOCUMENT IS UNLIMITED

108

1970

1970-1971

DISCLAIMER

This report was prepared as an account of work sponsored by an agency of the United States Government. Neither the United States Government nor any agency thereof, nor any of their employees, make any warranty, express or implied, or assumes any legal liability or responsibility for the accuracy, completeness, or usefulness of any information, apparatus, product, or process disclosed, or represents that its use would not infringe privately owned rights. Reference herein to any specific commercial product, process, or service by trade name, trademark, manufacturer, or otherwise does not necessarily constitute or imply its endorsement, recommendation, or favoring by the United States Government or any agency thereof. The views and opinions of authors expressed herein do not necessarily state or reflect those of the United States Government or any agency thereof.

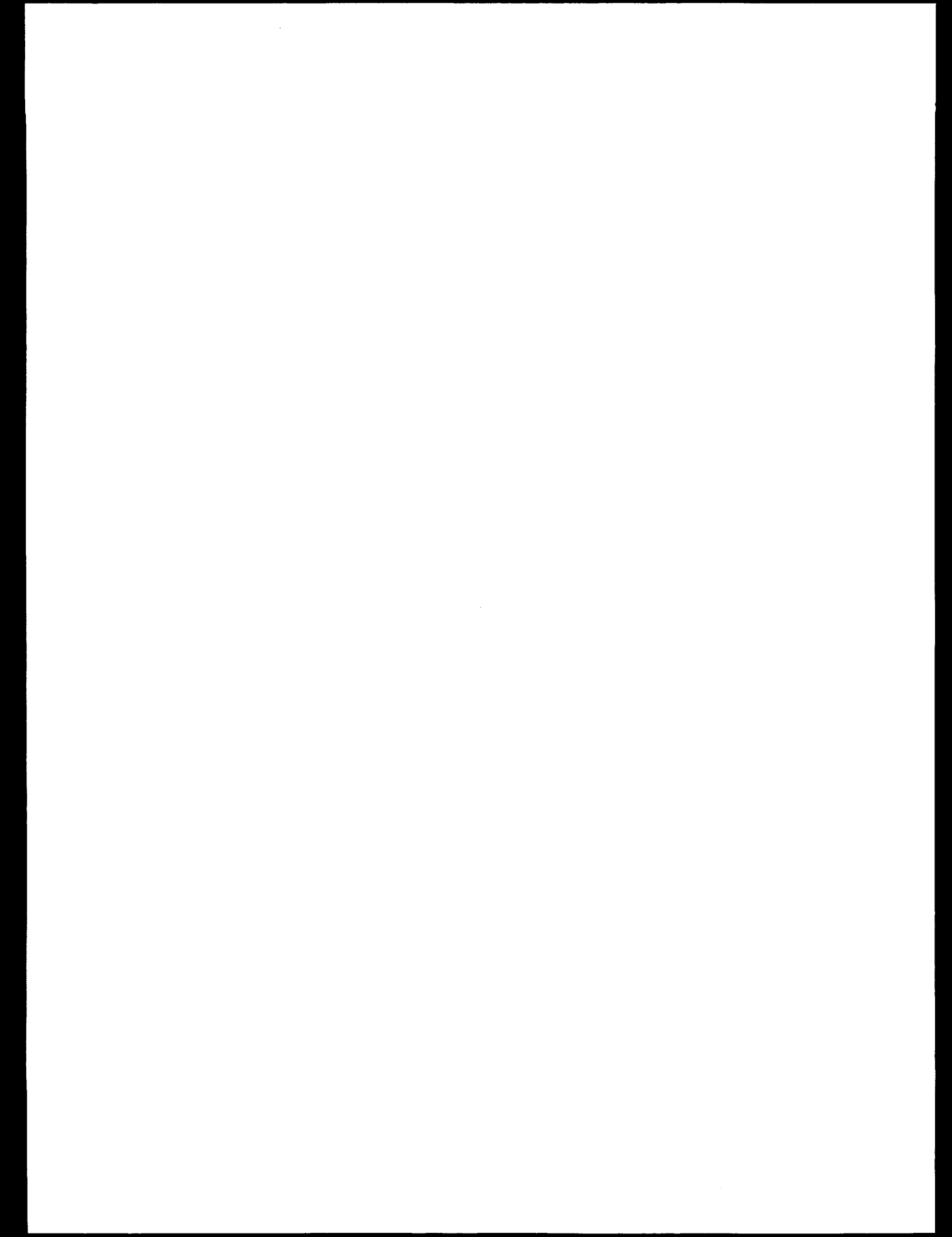
DISCLAIMER

**Portions of this document may be illegible
in electronic image products. Images are
produced from the best available original
document.**

ABSTRACT

During the period 1984–1987, researchers of the Heavy Section Steel Technology program at the Oak Ridge National Laboratory performed a unique series of fracture mechanics tests using exceptionally large, SE(T) specimens ($a/W = 0.2$) fabricated from a reactor pressure vessel material, A533B Class 1 steel. These “wide-plate” specimens have test sections of width $W = 1000$ mm, thickness $B = 100$ mm and initial crack lengths of 200 mm. While the specimen design, instrumentation and pre, post-test analyses focused on the cleavage run–arrest events, a disturbing outcome of the program centered on the inability of fracture mechanics analyses at that time to predict the loads required to initiate the first cleavage event — required loads exceeded twice those estimated from 3-D finite element analyses. The source of the much larger than expected initiation loads remained unresolved at completion of the wide-plate test program.

This study re-examines fracture initiation loads in the wide-plate tests using two constraint assessment methodologies developed over the past five years: the J – Q toughness locus approach and the toughness scaling approach based on a local failure criterion for cleavage. Both approaches demonstrate a significant loss of constraint in the elastic-plastic fields ahead of the crack in the wide-plate specimens caused by the inherent negative T -stress of the shallow notch SE(T) configuration. Moreover, the 25 mm wide machined notch required for specimen fabrication is shown to further reduce constraint by introducing a traction free surface very near the crack tip. Both of these factors combined to reduce near-tip stresses by 10% below those of the small-scale yielding, SSY ($T = 0$), fields. This reduction places fracture results for the wide-plate specimens within the J – Q toughness locus defined by fracture toughness tests on the A533B material and within the constraint corrected J_c values defined by the toughness scaling methodology.



Contents

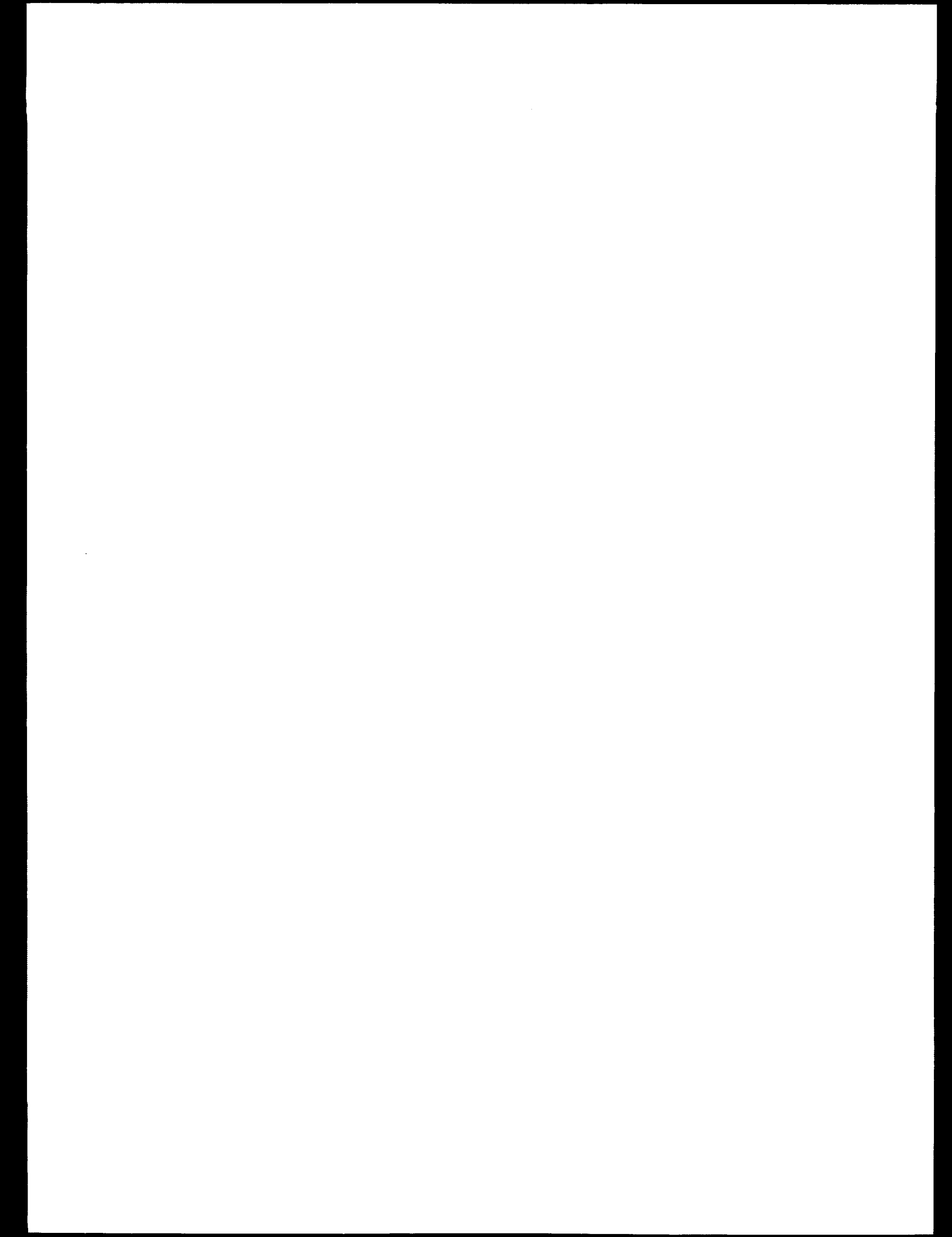
Section No.	Page
Abstract	iii
List of Figures	vi
List of Tables	vii
Acknowledgements	ix
1. Introduction	1
2. Overview of Wide-Plate Tests	2
2.1 Specimen Configurations	3
2.2 Material Characterization	4
3. Constraint Assessment Procedures	7
3.1 <i>J</i> - <i>Q</i> Theory	7
3.2 Toughness Scaling Model for Cleavage	10
4. Finite Element Analyses	13
4.1 Constitutive Model	13
4.2 Finite Element Models	14
4.3 Solution Procedures	14
4.4 Small-Scale Yielding Solutions	15
4.5 Effects of Side Grooves and Chevron Notching	16
5. Results and Discussion	17
5.1 Constraint Assessment Using <i>J</i> - <i>Q</i> Theory	18
5.2 Constraint Assessment Using Toughness Scaling Model	21
6. Summary and Conclusions	25
7. References	27
Appendix A	29

LIST OF FIGURES

Figure No.	Page
1 Schematic of HSST wide-plate crack-arrest specimen (WP-1 series)	3
2 Cleavage fracture toughness (J_c) results for wide-plate specimen(WP-1) material – Plate 13A, A533B3.	5
3 Cleavage fracture toughness (J_c) results for material – Plate 13B, A533B	5
4 Typical J - Q “loading paths” for fracture specimens and example construction of upper and lower limit toughness loci from measured J -values.	9
5 Effects of principal stress on predicted fracture toughness ratio, J_{FB}/J_0 , for a shallow notch SE(B) specimen.	11
6 Predicted effects of a/W ratio and absolute size on cleavage fracture toughness for SE(B) specimens.	13
7 Finite element models for analyses of wide-plate and fracture test specimens.	15
8 Opening mode stresses on crack plane for small-scale yielding ($T = 0$). Uniaxial σ - ϵ model is power-law hardening after an initial linear response (small-strain analyses).	16
9 Normalized J - Q driving force curves for wide-plate specimens and fracture test specimens. Computed using plane-strain analyses; no size corrections are included..	19
10 J - Q driving force curves and estimate of upper toughness locus for A533B material at -28°C . WP-1.3, SE(B) and C(T) fracture points are indicated.	20
11 J - Q driving force curves and estimates of toughness locus for A533B material at -10°C to $+10^\circ\text{C}$ (T - RT_{NDT}). WP-1.2, 1.5, 1.6, SE(B) and C(T) fracture points are indicated.	21
12 Normalized toughness scaling results for wide-plate specimens and fracture test specimens. (Scaling model curves constructed using opening mode stress on $\theta = 0$).	22
13 Constraint corrected toughness values (J_0) for wide-plate specimens and SE(B), C(T) test specimens. Gradients (m) for stationary constraint models of SE(B) specimens.	23
14 Effects of machined notch in wide-plate specimens on J - Q driving force curves.	24
15 Effects of machined notch in wide-plate specimens on constraint scaling model to estimate J_0	25

LIST OF TABLES

Table No.	Page
1 WP-1 series test specimen dimensions and measured values at cleavage fracture initiation from the pre-cracked configuration.	6
2 Mechanical properties for HSST A533B Class 1 Plates 13A and 13B.	6
3 Effective stresses, J_c - Q and J_0 values at fracture for plane-strain models of WP-1 series test specimens.	17
A.1 Fracture Test Data for A533B Plate 13A C(T) Specimens.	29
A.2 Fracture Test Data for A533B Plate 13B SE(B) Specimens.	30



ACKNOWLEDGEMENTS

This investigation was supported by a grant to the University of Illinois from the Oak Ridge National Laboratory, Heavy-Section Steel Technology program under Subcontract No. 19X-SM986V. Computations were performed on the Department of Civil Engineering HP/Apollo workstation network made possible, in part, by grants from the Hewlett-Packard Company.

The author acknowledges the many helpful conversations with Tim Theiss and Richard Bass of the HSST program and the comments provided by John Merkle.

1. Introduction

During the period 1984–1987, researchers of the Heavy Section Steel Technology program at the Oak Ridge National Laboratory performed a unique series of fracture mechanics tests using exceptionally large specimens [18][†]. The test program focused on understanding multiple cleavage run–arrest events in single edge notch tension, SE(T), specimens fabricated from a reactor pressure vessel material, A533B Class 1 steel. The “wide–plate” specimens, as they are now generally termed, comprise test sections of width $W = 1000$ mm, thickness $B = 100$ mm and initial crack lengths of 200 mm. End tabs, each 4 m in length, were welded to the $1\text{ m} \times 1\text{ m} \times 0.1\text{ m}$ test section to enable the application of pin loading. A steep temperature gradient imposed over the specimen width induced a corresponding toughness gradient, ranging from near lower–shelf conditions on the cold edge to upper–shelf conditions on the hot edge. Under remote tensile loading of these specimens, the crack initiates by cleavage in the low temperature region, propagates dynamically into material at higher temperature (and toughness) and eventually arrests when material toughness equals the dynamic driving force (multiple arrest and cleavage re–initiation events occurred in the tests).

While the specimen design, instrumentation and pre, post–test analyses focused on the cleavage run–arrest events, a disturbing outcome of the program centered on the inability of fracture mechanics analyses to predict the loads required to initiate the first cleavage event. In the earliest specimens, the required loads exceeded twice those estimated from 3–D finite element analyses (to estimate K_I) and from fracture toughness values obtained using 1–T and 2–T tests of conventional C(T) specimens. The unexpectedly high loads taxed the loading capacity of the system and precipitated a major nuisance in the experimental program. In subsequent tests, the crack–front thickness was reduced well below the 100 mm plate thickness with chevron notching in an effort to increase the effective K_I . In yet other specimens, the K_I generated by the remote tensile loading was supplemented with pressure loading applied directly to the crack faces using pillow jacks in addition to the chevron notching. These efforts realized only partial success. The source of the much larger than expected initiation loads remained unresolved at completion of the wide–plate test program.

Over the past five years, significant advancements have occurred in understanding the effects of specimen size, material flow properties and loading modes (tension, bending) on measured values of cleavage fracture toughness. Two complementary methodologies have evolved to quantify the effects of crack tip stress triaxiality (constraint) on the macroscopic measure of elastic–plastic fracture toughness, J . In the continuum mechanics methodology [19,20], two parameters, J and Q , suffice to characterize the full range of near–tip environments at the onset of fracture. J sets the size scale for the zone of high stresses and large deformations while Q scales the near–tip stress level relative to a high triaxiality reference stress condition of small–scale yielding (SSY). Full–field finite element calculations show that the J – Q field dominates over physically significant size scales, i.e., it describes the environment in which brittle and ductile failure mechanisms are active. The material’s fracture resistance is characterized by a toughness locus, $J_c(Q)$, which defines the sequence of J – Q values at fracture determined by experiment from high constraint conditions ($Q \approx 0$) to low constraint conditions ($Q < 0$). When specimens fracture under well–contained yielding, the complexity of a full–field nonlinear analysis becomes unnecessary; Q under such conditions is given quite accurately using the elastic T –stress for the specimen combined with a relatively simple, boundary layer analysis [21,6,12].

[†] Numbers in [] indicate references listed in Section 7.

The J - Q (and J - T) approach becomes prohibitively expensive as the number of specimens and temperatures of interest increases. To reduce the cost, a near-tip failure criterion for cleavage fracture [5,8] is introduced to predict the toughness locus using stress fields from finite element analyses and the J_c values from a few fracture toughness tests. Recent developments in the formulation of a robust and simpler model [2,10,11] focus on the observation of a strong similarity in the shapes of principal stress contours enclosing the crack tip under increased loading and across different fracture specimens. While the spatial variation remains self-similar, the sizes of principal stress contours vary dramatically as crack tip constraint evolves under loading (size refers here to distances from the tip along a ray at some angle θ). The near-tip criterion for cleavage fracture employs the volume of material bounded within principal stress contours around the crack tip at fracture to correlate J_c values for different specimens and loading modes, i.e., J_c values for different geometries/loading modes are scaled for the deterministic effects of constraint. The similarity in shapes of the principal stress contours as constraint evolves under loading is entirely consistent with the J - Q description of the crack tip stress fields. For an applied J -value, the size (but not the shape) of principal stress contours is altered by the near-tip, approximately hydrostatic stress states of adjustable magnitude characterized by Q .

This study re-examines the wide-plate tests using the J - Q and the toughness scaling methodologies to explain the unexpectedly large initiation loads at fracture. Both approaches demonstrate a significant loss of constraint in the elastic-plastic fields ahead of the crack caused by the inherent negative T -stress of the shallow notch SE(T) configuration. Moreover, the 25 mm wide machined notch required for specimen fabrication is shown to further reduce constraint by introducing a traction free surface very near the crack tip. Both of these factors combined to reduce near-tip stresses by 10% below those of the small-scale yielding, SSY ($T=0$), fields. This reduction places fracture results for the wide-plate specimens within the J - Q toughness locus defined by fracture toughness tests on the A533B material and within the constraint corrected J_c values defined by the toughness scaling methodology.

The contents of the paper are as follows: (i) an overview of the wide-plate test program and a subsequent test program which used the same material and large SE(B) specimens, (ii) development of the J - Q and toughness scaling methodology with sufficient detail for application to the wide-plate and fracture test specimens, (iii) finite element analyses performed on the wide-plate specimens and companion SE(B), C(T) fracture specimens to compute crack tip stresses and J -values needed for constraint assessments. The paper concludes with a detailed section which evaluates the wide-plate specimens using these two methodologies.

2. Overview of Wide-Plate Tests

The first wide-plate test program (series WP-1, [18]) investigated the run-arrest behavior of cracks in large plates possessing steep toughness gradients. Test sections of size 1 m \times 1 m \times 0.1 m were fabricated from A533B Class 1 steel plate as single-edge notch fracture specimens loaded by a remotely applied tensile force. Initial crack depth-to-specimen width ratios (a/W) of nominally 0.2 were tested. A linear temperature profile was imposed across the 1 m wide plate to develop the steep toughness gradient. The crack initiated by cleavage on the low temperature side, propagated dynamically into material at higher temperature (and toughness) and eventually arrested when material toughness equaled the dynamic driving force. Extensive instrumentation on the specimens recorded the crack initiation and propagation events. Post-test analyses revealed a complex sequence of initiation \rightarrow run \rightarrow arrest \rightarrow reinitiation events.

This section summarizes the specimen configurations and material properties of the wide-plate tests relevant to the present investigation of the much larger (than expected) loads required to initiate the first cleavage event. Complete details of the fabrication, testing procedure and material characterization are provided in [18].

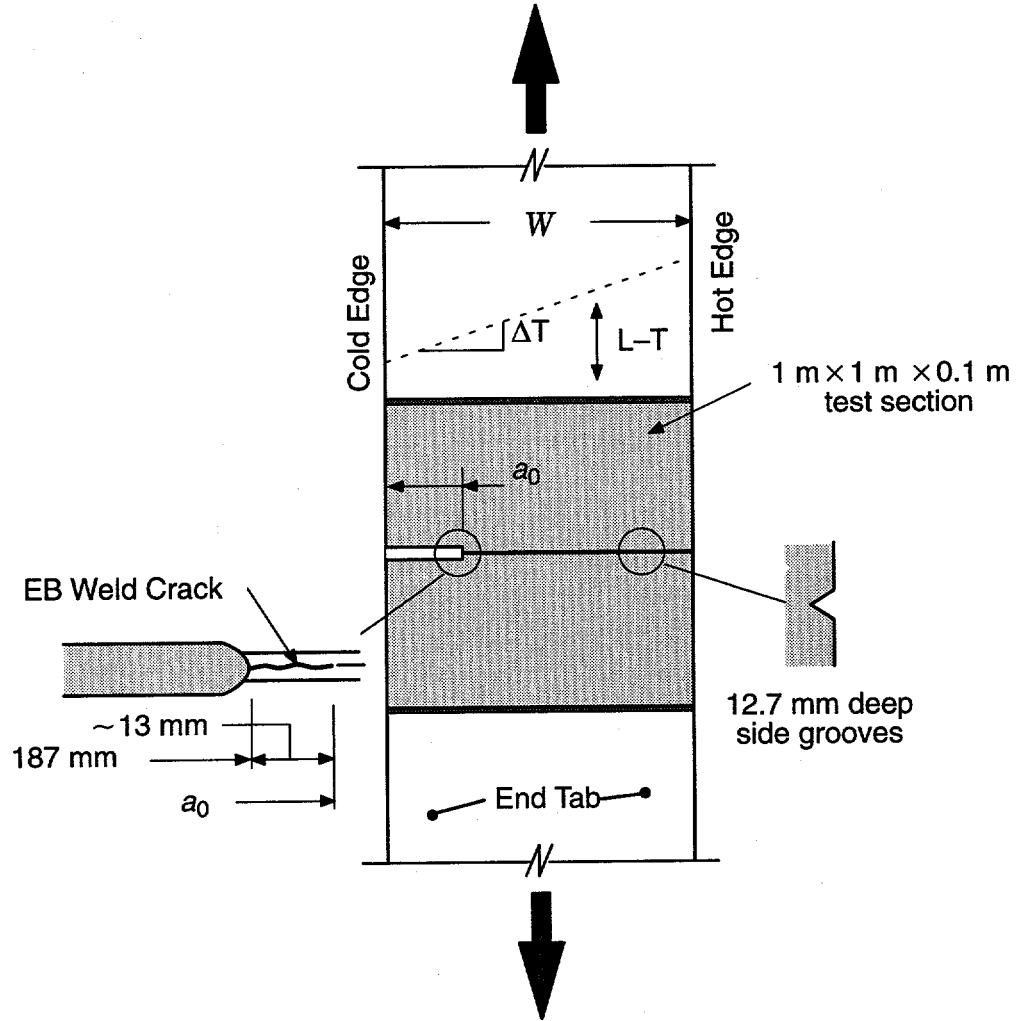


Figure 1 Schematic of HSST wide-plate crack-arrest specimen (WP-1 series).

2.1 Specimen Configurations

Figure 1 shows the overall specimen design with the $1 \text{ m} \times 1 \text{ m} \times 0.1 \text{ m}$ test section welded to end tabs through which the pin loading was applied. In the WP-1 series, six such specimens were fabricated and tested (designations WP-1.1 through WP-1.6). Precracking was performed by hydrogen charging of an electron beam (EB) weld located at the base of a machined notch (187 mm long by 25.4 mm wide). This procedure generated a sharp-tipped crack of ~ 13 mm in length at the end of the machined notch. The 187 mm long notch, terminated by the 13 mm crack, provided an overall specimen crack length of nominally 200 mm for an $a_0/W \approx 0.2$. Side grooves with depth 12.7 mm were employed in all six specimens. The crack plane is perpendicular to the rolling direction (L-T orientation).

Table 1 summarizes the dimensions for the four specimens examined in the present study (WP-1.2, 1.3, 1.5, 1.6). Testing procedures for specimens WP-1.1 and 1.4 introduced additional complications: WP-1.1 underwent a warm prestress cycle; WP-1.4 had crack face loading applied by a pillow jack in addition to the remote tensile loading. This work omits consideration of these two specimens.

The unexpectedly large load required to initiate the first cleavage event in WP-1.2 prompted the introduction of chevron notches at the crack front in subsequent specimens. Chevron notching reduced the plate thickness at the crack front by $\sim 50\%$ in specimens WP-1.3, 1.5 and 1.6. Three-dimensional, linear-elastic finite element analyses conducted prior to these tests predicted a 35% increase in applied K_I at mid-thickness relative to the WP-1.2 specimen (no chevron notching).

Table 1 also provides the measured crack-front temperatures and measured loads at initiation of the first cleavage fracture event for the four test specimens (WP-1.2, 1.3, 1.5, 1.6). Additional columns provide: the nominal axial stress at fracture (neglecting side-grooves), the mid-thickness K_I at fracture (computed using geometry factors from the linear, 3-D finite element analyses and measured fracture loads), and the ratio of K_I at fracture to K_{Ic} (applicable K_{Ic} values derived from pre-test fracture characterization studies conducted on compact tension specimens). The large K_I/K_{Ic} ratios (> 2) remained unexplained at conclusion of the wide-plate test program.

2.2 Material Characterization

The $1\text{ m} \times 1\text{ m} \times 0.1\text{ m}$ test sections of specimens in the WP-1 program were taken from the same HSST plate of A533B steel, designated Plate 13A. A single manufactured Plate 13 was divided into plates 13A, 13B to facilitate shipment and further fabrication. Plate 13A was quenched and tempered, then stress relieved which produced exceptionally uniform, through-thickness properties. Table 2 lists the mechanical properties for Plate 13A at -40°C . Multi-linear models for the uniaxial, tensile stress-strain curve over a range of temperatures are also available (see Fig. 4.4 and Table 4.2 of [18]). In the finite element analyses described later in this report, a power-law hardening representation following an initial linear response is adopted with the hardening exponent taken as $n = 10$. The RT_{NDT} (ASME reference nil-ductility temperature) is -23°C as measured by drop weight/Charpy testing in the L-T orientation.

Nineteen compact tension tests, 1T-C(T) and 2T-C(T) with $a/W \approx 0.55$, were fabricated from Plate 13A material and tested to quantify fracture toughness over the ductile-to-brittle transition (DBT) region. Additional tests were performed at higher temperatures to characterize the R -curve for the material. Test temperatures ranged from -150°C to -18°C ; all of these tests terminated in cleavage, with the development of significant ductile crack extension prior to cleavage at only the highest temperatures. Figure 2 shows the measured J_c values (J at cleavage fracture). Specimens with 0.1 mm or greater of ductile tearing prior to cleavage are highlighted.

A recent HSST investigation [27,4] has examined the shallow crack effect on fracture toughness by testing single-edge notched beams, SE(B)s, taken from HSST Plate 13B. This plate received a heat treatment similar to Plate 13A used for the WP-1 test program. Table 2 lists the mechanical properties measured at -40°C . The RT_{NDT} is -15°C for this material compared to -23°C for Plate 13A. Eighteen SE(B) specimens with $W = B = 102\text{ mm}$ and span of 610 mm were tested over a range of temperatures in three-point bending. Six specimens had deep cracks ($a/W = 0.5$); the remaining twelve specimens had shallow cracks ($a/W = 0.1$). Figure 3 shows the measured J_c values for the eighteen SE(B) specimens. Measurements of ductile tear-

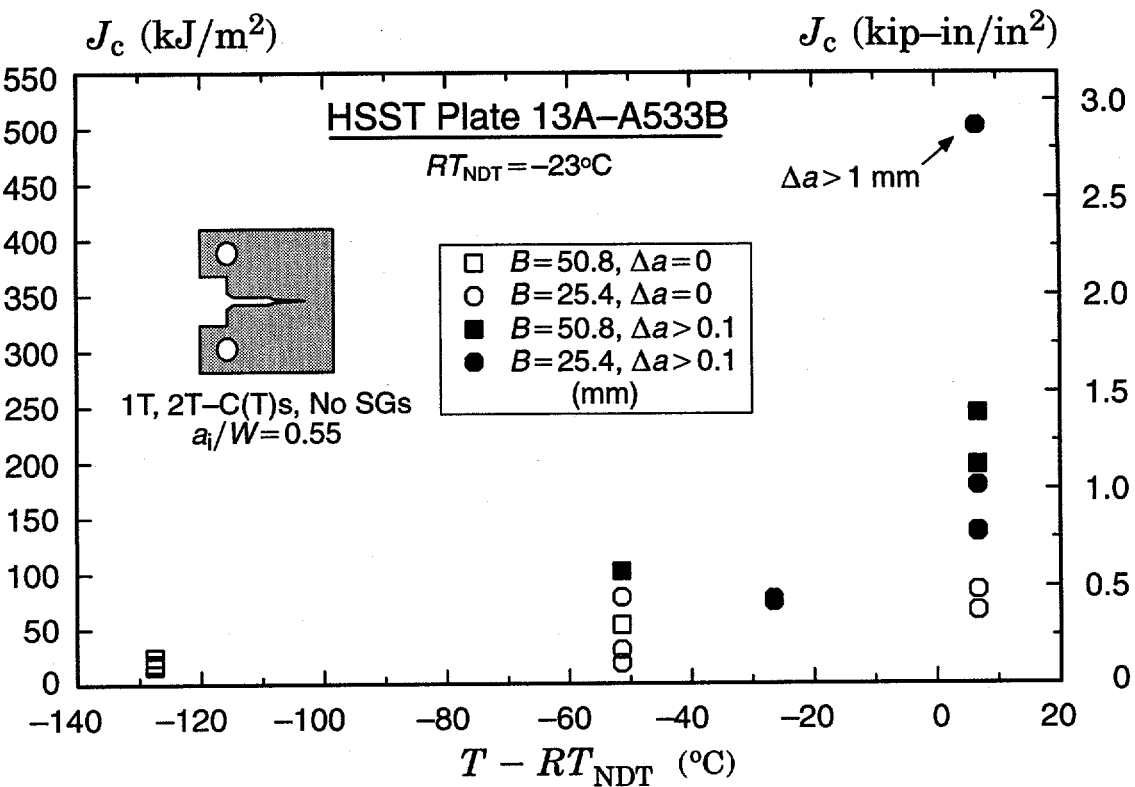


Figure 2. Cleavage fracture toughness (J_c) results for wide-plate specimen (WP-1) material – Plate 13A, A533B [18].

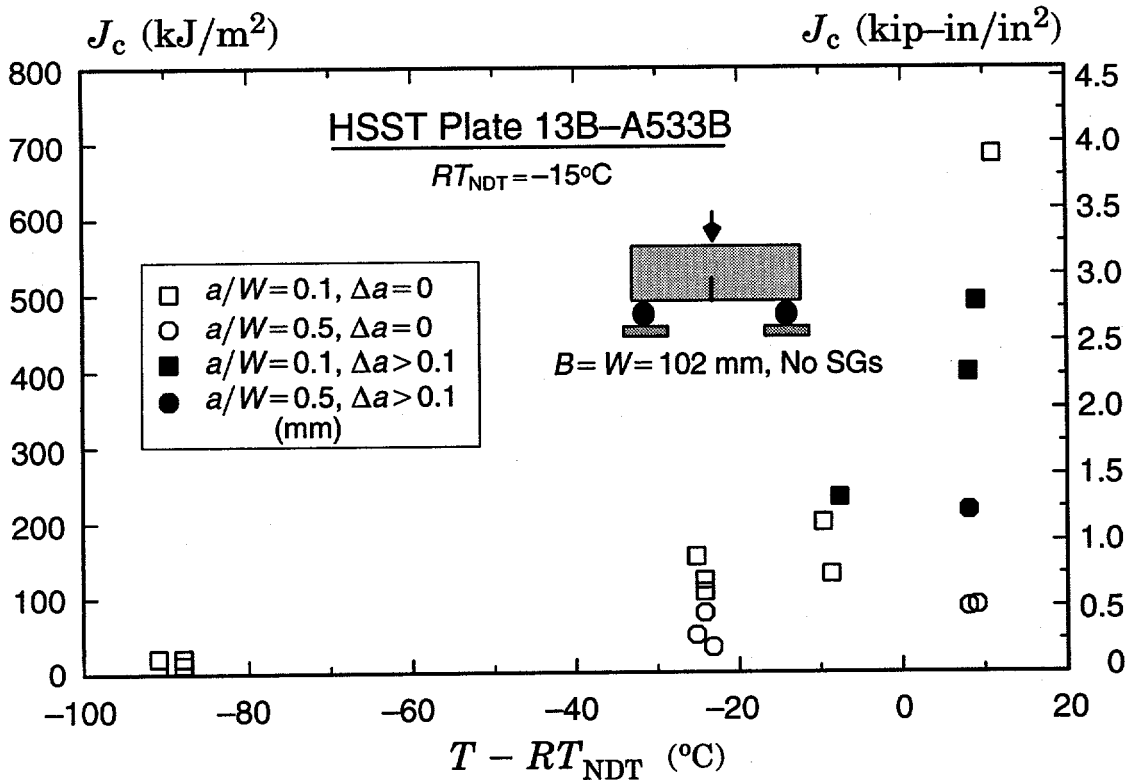


Figure 3. Cleavage fracture toughness (J_c) results for material – Plate 13B, A533B [27,4].

ing prior to cleavage are available for 6 of the specimens; in each of these cases $\Delta a < \delta_c$ (the estimated CTOD at cleavage). In terms of J_c , the shallow crack specimens exhibit a *mean* toughness $2.5 \times$ the *mean* toughness of the deep notch specimens for tests conducted in the transition range, $T-RT_{NDT} = -25$ to $+10^\circ\text{C}$. At temperatures on the lower-shelf of the DBT curve, there is no shallow crack effect (both deep and shallow specimens fracture under conditions of small-scale yielding and “valid” ASTM E399 [3] toughness values, K_{Ic} , are measured). To simplify subsequent discussions of constraint effects on the fracture loads of the wide-plate tests, the J_c values measured using C(T) and SE(B) specimens from Plates 13A and 13B given in Figs. 2, 3 are combined into a single data set with temperatures referenced to RT_{NDT} .

Table 1. WP-1 series test specimen dimensions and measured values at cleavage fracture initiation from the pre-cracked configuration [18].

Quantity	Specimen Designation			
	WP-1.2	WP-1.3	WP-1.5	WP-1.6
Width (W , mm)	998	1000	1000	1000
Initial crack length (a_0 , mm)	199	197	200	200
Thickness (B , mm)	101.8	99.5	101.7	101.8
Notched thickness (B_N , mm)	77.5	75.4	76.4	75.5
Chevron thickness (B_C , mm) (thickness at a_0)	*	47.5	41.2	40
Crack front temp. (T_f , $^\circ\text{C}$)	-33	-51	-30	-19
Crack front temp. (T_f-RT_{NDT} , $^\circ\text{C}$)	-10	-28	-7	4
Fracture load (P_f , MN)	18.9	11.25	11.03	14.5
Stress at fracture (σ^∞ , MPa)	186	113	108.5	142.5
K_I at fracture (MPa $\cdot \sqrt{\text{m}}$)	252	174	180	232
K_I/K_{Ic}	2.9	2.5	2.0	2.1

*Chevron not used

Table 2. Mechanical properties for HSST A533B Class 1 Plates 13A and 13B [18,27].

Property	HSST A533B Plate Designation	
	13A (@ -40°C)	13B (@ -40°C)
Young's modulus (E , GPa)	209.5	207.2
Poisson's ratio (ν)	0.3	0.3
Yield stress (σ_0 , MPa)	457	454
Ultimate stress (σ_u , MPa)	650	640
Flow stress (σ_{fl} , MPa)	553	547
Nil-ductility temp. (RT_{NDT} , $^\circ\text{C}$)	-23	-15

3. Constraint Assessment Procedures

In fracture test specimens and structural components, both subjected to low levels of loading, crack tip plastic zones remain "small" relative to the crack length, ligament length and thickness. Under such conditions, often termed small-scale yielding (SSY), there exists a unique coupling between load, J , K_I and the near tip strain-stress fields. A single fracture parameter (K_I or J) suffices to describe both the near tip fields and the measured fracture toughness. However, under increased load, the SSY fields gradually breakdown as the crack tip plastic zones interact with nearby traction free boundaries; the crack tip fields are no longer uniquely described by J or K_I , and the measured fracture toughness becomes a complex function of specimen geometry, loading mode and material flow properties.

Considerable recent work [19–12,2–31] in fracture mechanics focuses on quantifying these kinematic effects of plastic flow at the crack tip to predict the influence on fracture toughness. Two approaches of interest here are the J – Q theory to describe crack tip fields as developed by O'Dowd and Shih [19,20] and the constraint model to scale cleavage fracture toughness developed by Dodds and Anderson[2,10,11]. Both approaches quantify the level of loading (relative to specimen size, crack size, and material flow properties) when global plasticity impinges on the SSY crack tip fields.

The J – Q theory provides an approximate two-parameter description of the elastic-plastic crack tip stress and strain fields. J scales with the global loading and defines the local crack tip deformation ($CTOD \propto J/\sigma_0$); Q scales the level of stress triaxiality over the relevant fracture process zones ahead of the crack tip ($1–5 \times CTOD$). Material toughness (cleavage or initiation of ductile tearing) becomes a function of both J at fracture and Q at fracture; different specimen geometries and loading modes produce a variety of J – Q "loading paths" which lead to a J – Q toughness *locus* connecting measured fracture points on such paths.

In the Dodds and Anderson approach, constraint effects on fracture toughness are quantified by coupling the global failure parameter (J_c) with a local failure criterion for cleavage. The model is designed for ferritic materials operating in the ductile-to-brittle transition region when fracture occurs by a stress-controlled, transgranular cleavage mechanism. The near tip stress field at fracture in a common test specimen, typically an SE(B) with $a/W = 0.5$, is correlated through finite element analyses to other specimens to predict the relative J -values at fracture. The criterion requires a common intensity of crack tip stress fields at fracture in all specimens even though the J values may differ significantly. By adopting a specific fracture mechanism (stress-controlled cleavage), the effects of stress triaxiality (Q) are reflected in the measured/predicted values of fracture toughness (J_c). Extensive testing required to generate a toughness locus is reduced but with a loss of generality – the transition between a ductile tearing and cleavage mechanism cannot be predicted by the model.

The following sections outline essential features of the J – Q and the Dodds–Anderson approaches for constraint assessment needed to evaluate the wide-plate tests.

3.1 J – Q Theory

The J – Q description of Mode-I, plane-strain crack tip fields derives initially from consideration of the modified boundary layer (MBL) solution [7] which expresses near tip stresses for linear elastic, conditions in the form [32],

$$\sigma_{ij} = \frac{K_I}{\sqrt{2\pi r}} \tilde{f}_{ij}(\theta) + T\delta_{1i}\delta_{1j} . \quad (1)$$

Here r and θ are polar coordinates centered at the crack tip with $\theta = 0$ corresponding to a line ahead of the crack. Crack tip fields differing in stress triaxiality are generated by varying the non-singular stress, T , parallel to the crack plane. Within the plane-strain MBL formulation,

$$J = \frac{1 - \nu^2}{E} K_I^2 \quad (2)$$

where J is Rice's J -integral [23], E is Young's modulus and ν is Poisson's ratio.

In the computational model for small-scale yielding, the conditions defined by Eq (1) are imposed incrementally on the remote outer boundary of a symmetrically constrained, semi-circular mesh of elements focused on the crack tip. When the plastic zone remains small relative to the extent of the modelled region, the non-singular T -stress term does not affect computed values of J , as implied by Eq (1). However, Larsson and Carlsson [16] were the first to demonstrate that the second term significantly alters the plastic zone shape and size as well as stresses ahead of the crack tip. These elastic-plastic crack tip fields can be organized into a family of fields parameterized by T/σ_0 :

$$\sigma_{ij} = \sigma_0 \bar{f}_{ij} \left(\frac{r}{J/\sigma_0}, \theta; T/\sigma_0 \right), \quad (3)$$

where σ_0 is the tension yield stress of the material. Subsequent work by Leevers and Radon [17], Bilby, et al. [7] and more recently by Betegon and Hancock [6], Wang and Parks [31] and others have explored the applicability of this $J-T$, MBL description of crack tip fields in fracture specimens; the appeal being the simplicity of estimating an elastic-plastic value for J and an elastic value for T . This methodology proves quite successful [14] in well-contained yielding, especially for specimen geometries which exhibit very high constraint (large *positive* T -stresses; deep notch bend, compact tension, $a/W \geq 0.5$) and very low constraint (large *negative* T -stresses; middle crack tension, shallow notch bend, $a/W \leq 0.2$). However, the elastic T -stress, which increases proportionally with K_I , becomes ambiguous under conditions of large-scale yielding as K_I saturates to a constant value at limit load.

O'Dowd and Shih [19,20] employed asymptotic and finite element analyses to develop an approximate two-parameter description of the crack tip fields without the limitations of the T -stress,

$$\sigma_{ij} = \sigma_0 f_{ij} \left(\frac{r}{J/\sigma_0}, \theta; Q \right), \quad (4)$$

$$\varepsilon_{ij} = \varepsilon_0 g_{ij} \left(\frac{r}{J/\sigma_0}, \theta; Q \right). \quad (5)$$

The dimensionless second parameter, Q , in Eqs (4,5) defines the mechanism by which σ_{ij} and ε_{ij} in fracture specimens differ from the adopted SSY ($T = Q = 0$) reference solution at the same applied- J . For non-zero values of the T -stress, Q and T exhibit a one-to-one correspondence in SSY that varies only with the material flow properties [21].

Through extensive 2-D finite element analyses, O'Dowd and Shih showed that, to a good approximation, $Q\sigma_0$ represents the *difference* of the hydrostatic stress between SSY($T = 0$) and fracture specimens over the forward sector ahead of the crack tip,

$$\sigma_{ij} = (\sigma_{ij})_{SSY,T=0} + Q\sigma_0 \delta_{1i} \delta_{1j}; \quad |\theta| < \frac{\pi}{2}, \quad J/\sigma_0 < r < 5J/\sigma_0. \quad (6)$$

Operationally, Q is defined by

$$Q \equiv \frac{\sigma_{\theta\theta} - (\sigma_{\theta\theta})_{SSY;T=0}}{\sigma_0}, \quad \text{at } \theta = 0, r = 2J/\sigma_0 \quad (7)$$

where the specimen stresses $(\sigma_{\theta\theta})$ in Eq (7) are evaluated from finite element analyses containing sufficient mesh refinement to resolve the fields at this length scale (where the fracture specimen and SSY are loaded to the same J). Values of Q derived from small-displacement, small-strain analyses are adequate for most applications.

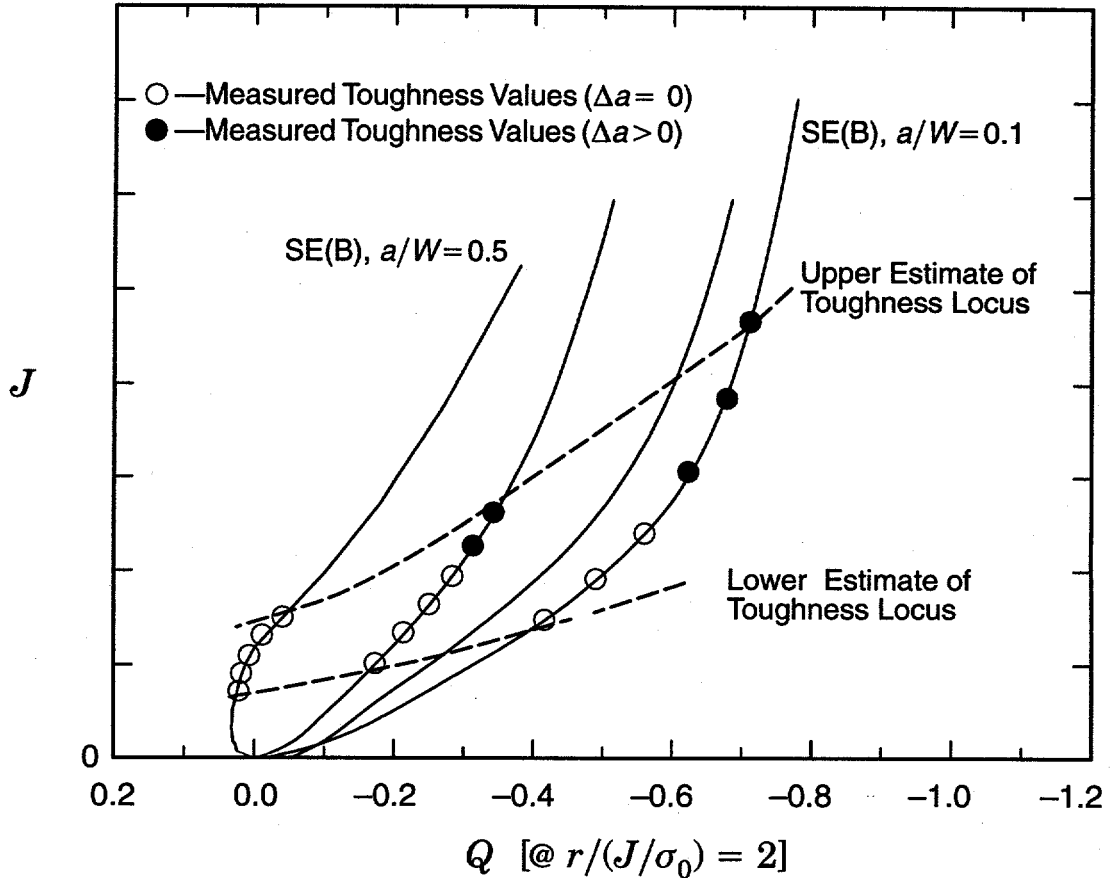


Figure 4. Schematic of J - Q "loading paths" for fracture specimens and example construction of upper and lower limit toughness loci from measured J -values.

Figure 4 shows typical J - Q "loading paths" for several types of fracture specimens. Additional examples of J - Q loading paths, including those at locations along the curved front of a surface cracked plate, are available [11,13]. At low deformation levels ($J \rightarrow 0$), the fracture specimens experience SSY ($T \approx 0$) conditions and Q remains very nearly zero (Q and T are uniquely related under SSY and $T \propto K_I$). Once large-scale yielding conditions prevail, hydrostatic stresses at the crack tip are substantially less than those in SSY ($T \approx 0$) at the same J -value. This difference produces negative Q values once the specimen deviates from SSY conditions. For deeply notched SE(B) and C(T) specimens, the elastic T -stress is positive and thus Q takes on slightly positive values at low deformation levels before constraint loss occurs.

Testing of fracture specimens enables construction of the J - Q toughness locus for a material at a specified temperature. The test program should utilize fracture specimens that generate

high, intermediate, and low constraint in terms of J - Q loading paths. Experimentally measured J -values at fracture (cleavage or ductile initiation) are plotted on the loading paths computed by finite element analyses for the specimens. The Q -value at fracture is thus not measured; it is determined from the position of J at fracture on the loading path. The usual scatter in results observed for multiple tests of the same specimen configuration defines points that lie along the loading path for that specimen (Fig. 4 illustrates this). By connecting, separately, the upper-most fracture value on all loading paths tested and then the lower-most fracture values, estimates for practical upper and lower bound toughness loci may be constructed. The potential overlap of cleavage and ductile initiation results on the upper and lower loci define constraint levels required to alter the fracture mode (cleavage under high constraint and tearing under low constraint). Lower and upper estimates of fracture loads for another type of specimen or structural component are predicted using toughness values defined at the intersection of the specimen/component's computed J - Q loading path with the material's lower and upper toughness locus.

3.2 Toughness Scaling Model for Cleavage

Dodds and Anderson quantify the geometric effects on fracture toughness by coupling the global fracture parameter (J_c) with a near-tip failure criterion. The model addresses ferritic materials operating in the ductile-to-brittle transition region which fracture by transgranular cleavage. For this failure mechanism, several models have been proposed [24–30]. These models assume a favorably oriented particle (e.g. carbide or inclusion) initiates cleavage fracture. Failure of this particle creates a microcrack which triggers global fracture through a local Griffith instability. The stochastic sampling effects of locating a favorably oriented particle to trigger the initial microcrack suggest that the highly stressed volume of material in the forward sector ahead of the crack plays a dominant role.

These features led to adoption of the material volume ahead of the crack tip over which the normalized (maximum) principal stress, σ_1/σ_0 , exceeds a critical value as the local failure criterion. Unlike previous local models for cleavage fracture, the present methodology does not attempt to predict values of J_c from metallurgical parameters that describe the distribution and strength of cleavage triggering particles. Rather, this model predicts the variation of fracture toughness with constraint changes for a specified material/temperature by scaling to a common reference condition.

By employing the family of near-tip states in the form of Eq (6), the maximum principal stress also has the (approximate) form

$$\frac{\sigma_1}{\sigma_0} = f_0\left(\frac{r}{J_0/\sigma_0}, \theta\right) + Q . \quad (8)$$

For any given value of Q and θ , σ_1/σ_0 decreases monotonically once r extends beyond the finitely deformed region of $r \leq J/\sigma_0$. Rearrangement of the above expression furnishes a relation for the distance r as a function of θ and σ_1/σ_0 as

$$r = \frac{J}{\sigma_0} g_1(\theta; \sigma_1/\sigma_0, Q) . \quad (9)$$

Consider now a particular level of the principal stress σ_1/σ_0 . The area A over which the principal stress is greater than σ_1/σ_0 is given by

$$A = \frac{J^2}{\sigma_0^2} h(\sigma_1/\sigma_0; Q), \quad h = \frac{1}{2} \int_{-\pi}^{\pi} g_1^2(\theta; \sigma_1/\sigma_0, Q) d\theta . \quad (10)$$

The area enclosed by the contour of level σ_1/σ_0 depends on J as well as the triaxiality of the near-tip fields identified with Q . To fix ideas, let A_0 and J_0 designate the area and J associated with the $Q=0$ field (SSY, $T=0$), and let A_{FB} and J_{FB} designate the area and J associated with a crack in a finite body with $Q \neq 0$. Then we have

$$A_0 = \frac{J_0^2}{\sigma_0^2} h_0(\sigma_1/\sigma_0); \quad h_0 = \frac{1}{2} \int_{-\pi}^{\pi} g_1^2(\theta; \sigma_1/\sigma_0, Q=0) d\theta \quad (11a-b)$$

and

$$A_{FB} = \frac{J_{FB}^2}{\sigma_0^2} h_{FB}(\sigma_1/\sigma_0); \quad h_{FB} = \frac{1}{2} \int_{-\pi}^{\pi} g_1^2(\theta; \sigma_1/\sigma_0, Q) d\theta . \quad (12a-b)$$

Upon initial loading of the finite body, $Q=0$ so that $h_{FB}=h_0$; compare Eqs (11b) and (12b). As the load increases, plasticity spreads over the body, Q becomes non-zero, and h_{FB} begins to deviate from h_0 .

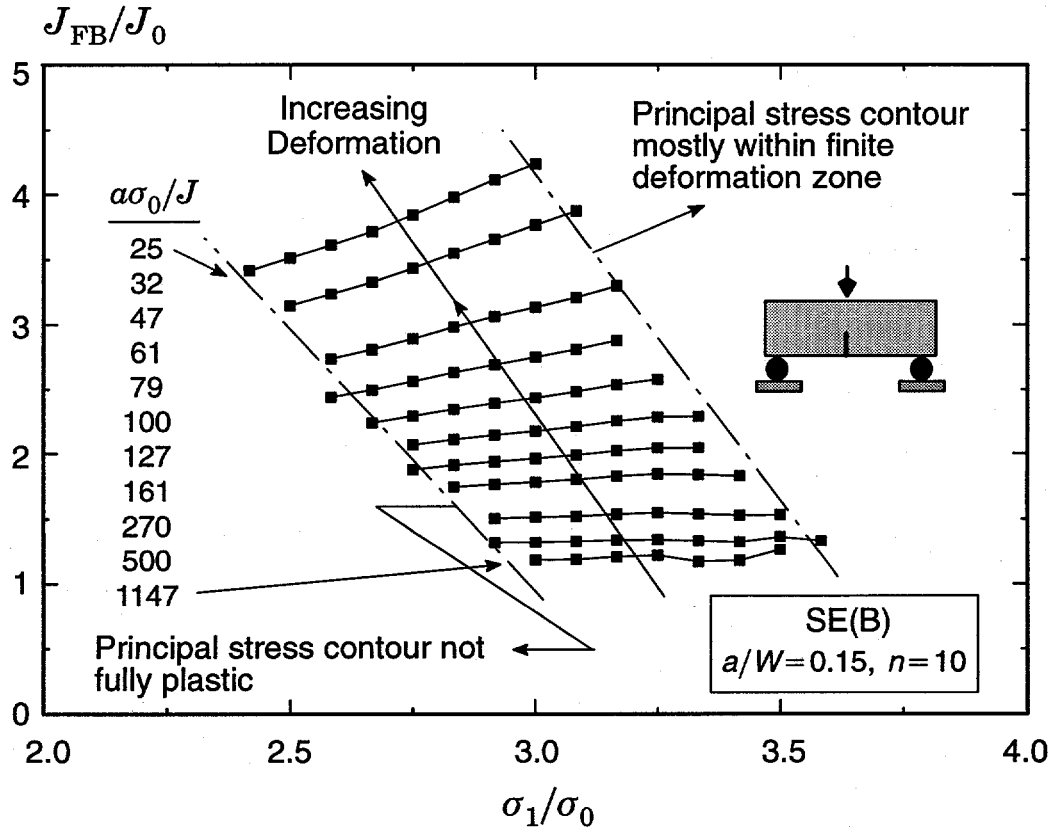


Figure 5. Effects of principal stress on predicted fracture toughness ratio, J_{FB}/J_0 , for a shallow notch SE(B) specimen.

For the same material and specified temperature, the present model requires attainment of equivalent stressed volumes ($A_{FB} \times$ thickness, B) for triggering of cleavage fracture in different specimens, i.e., once the stressed volumes are equal so are the *probabilities* for triggering cleavage fracture). The ratio of applied J -values in a finite body and the reference $Q = 0$ stress state that generate equivalent stressed volumes is found by equating areas in Eqs (11a) and (12a) to yield

$$\frac{J_{FB}}{J_0} = \sqrt{\frac{h_0(\sigma_1/\sigma_0)}{h_{FB}(\sigma_1/\sigma_0)}} = \sqrt{\frac{A_0(\sigma_1/\sigma_0)}{A_{FB}(\sigma_1/\sigma_0)}}. \quad (13)$$

The J ratios are evaluated using Eq (13) at each loading level and for a range of principal stress values. The ratio quantifies the size and geometry dependence of cleavage fracture toughness. A critical value of J_0 represents the fracture toughness of an infinitely large specimen (SSY, $T = 0$); a $J_{FB}/J_0 > 1$ implies that the specimen has experienced a constraint loss that causes the commonly observed increase in measured fractured toughness. Consider, for example, a test specimen that fails at $J_c = 200 \text{ kJ/m}^2$ and the computed ratio $J_{FB}/J_0 = 2$ at fracture ($J_{FB} = J_c$) in the test specimen; then a very large specimen (assumed to be in SSY) made from the same material and tested at the same temperature is predicted to fail at $J_c = 100 \text{ kJ/m}^2$. Similarly, the fracture toughness ratios for test specimens with the same absolute size but varying crack-depth to specimen-width, a/W , may be quantified. The model predicts a sharp increase in fracture toughness with decreasing a/W ratio.

Computational studies of SSY with $T \neq 0$ and of various fracture specimens often reveal a noticeable independence of the J_{FB}/J_0 ratio on the selected σ_1/σ_0 (which must be sufficiently large, e.g., > 2 , so that the contour lies entirely in the forward sector and in the plastic zone). Figure 5 illustrates the variation of J_{FB}/J_0 with σ_1/σ_0 for a shallow notch SE(B) specimen. The J - Q description of the principal stresses given by Eq (8) implies that the *shape* of principal stress contours (the f_0 function) is maintained while the relative *magnitude* of the contours varies directly with the hydrostatic stress $Q\sigma_0$. This *self-similarity* of principal stress contours prevails only to the extent that the approximate J - Q description of the crack tip stresses remains valid. At very large-scale yielding, particularly for specimens subjected to severe global bending, the similarity breaks down and J_{FB}/J_0 varies strongly with σ_1/σ_0 (Fig. 5 shows this behavior at the largest load levels $a\sigma_0/J < 30$).

The computational procedures outlined above have been applied to generate J_{FB}/J_0 ratios for a variety of test specimens (including surface cracked specimens) and material properties [2–11,13]. Figure 6 provides the results of such computations for SE(B) specimens having a range of a/W ratios modelled with an $n = 5$ strain hardening material. Values of J_{FB} and J_0 are plotted on separate axes to facilitate removal of the size effect in experimental data. Points on the curves describe (J_{FB}, J_0) pairs that produce equal stressed volumes of material in the test specimen and in the SSY model. Upon initial loading, crack tip plasticity is well contained within a surrounding elastic field and identical values for J_{FB} and J_0 correspond to the same stressed volume of material at the crack tip. This 1:1 line is shown on the figure for reference. At higher loads and as constraint relaxes under extensive plastic flow, the test specimen requires more applied- J ($J_{FB} > J_0$) to achieve the same conditions for cleavage (same stressed volume) as in SSY.

Information of this type is useful for both analysis of fracture test data and for assessing the defect integrity of structures. Path A–B–C shown in Fig. 6 illustrates the procedure to remove geometry dependence from experimental cleavage fracture toughness data (J_c value at A) by determining the geometry independent cleavage fracture toughness (J_0 value at C) corre-

sponding to a measured J_c value. Alternatively, Fig. 6 permits determination of the apparent fracture toughness for an SE(B) with any a/W ratio from a known J_0 value (path C-D-E for example).

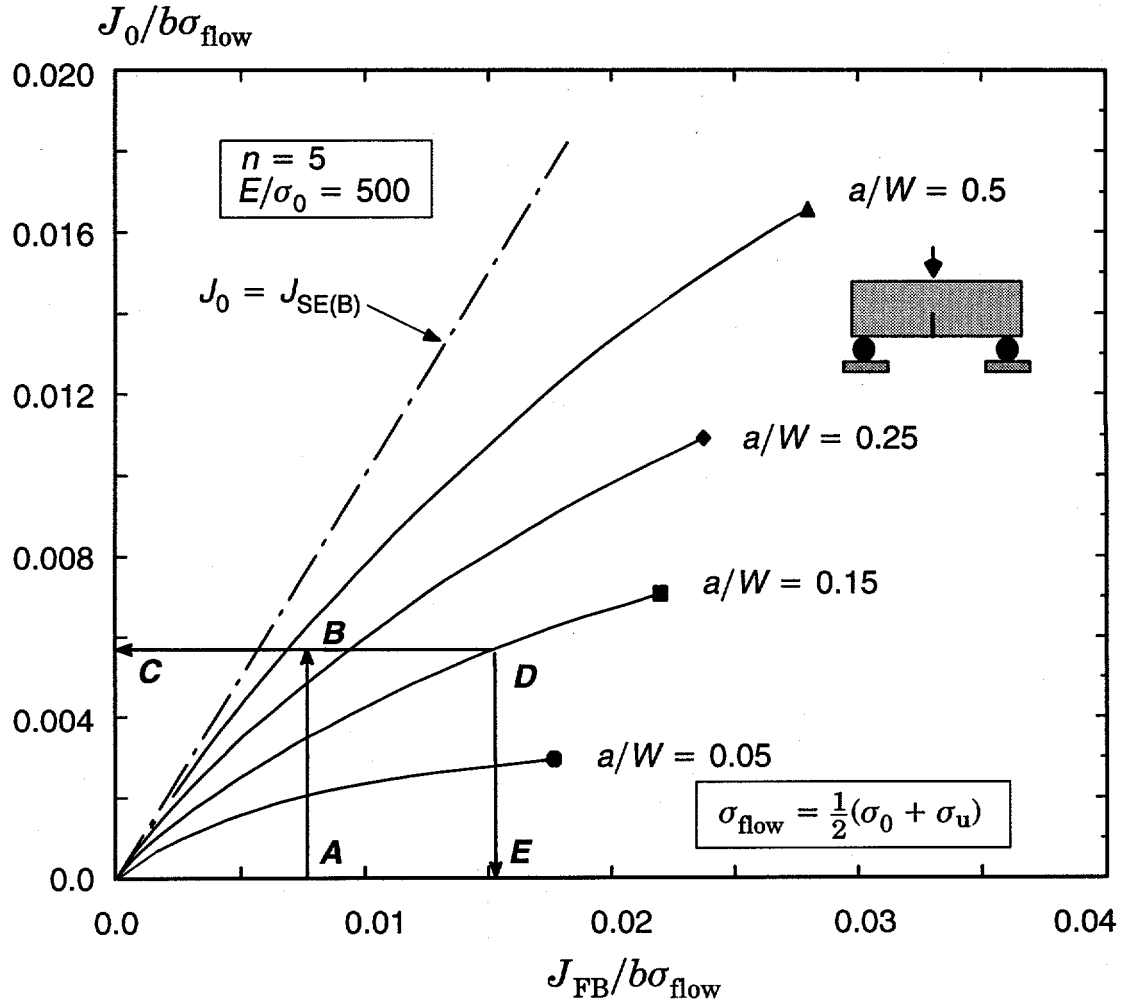


Figure 6. Predicted effects of a/W ratio and absolute size on cleavage fracture toughness for SE(B) specimens.

4. Finite Element Analyses

Plane-strain finite element analyses were performed to obtain detailed descriptions of the crack tip stress fields for the wide-plate specimens and for the fracture specimens used in the material testing programs—SE(B) with $a/W = 0.1, 0.5$ for Plate 13B material and C(T) with $a/W = 0.6$ for Plate 13A material. The SSY solutions for stresses on the crack plane needed to evaluate Q and toughness ratios, J_{FB}/J_0 , in these geometries are summarized. The remainder of this section outlines the details of the models, solution procedures and the approach developed to represent the effects of side grooves and chevron notches.

4.1 Constitutive Model

The material model employs J_2 deformation plasticity theory (nonlinear elasticity) in a conventional small-strain setting. The uniaxial stress-strain curve follows a linear then power-law model given by

$$\frac{\varepsilon}{\varepsilon_0} = \frac{\sigma}{\sigma_0} \quad \varepsilon \leq \varepsilon_0 \quad (14)$$

$$\frac{\varepsilon}{\varepsilon_0} = \left(\frac{\sigma}{\sigma_0} \right)^n \quad \varepsilon > \varepsilon_0 \quad (15)$$

where ε_0 and σ_0 define limits for the initial linear portion of the response. A small, cubic transition region eliminates the discontinuous tangent modulus at $\varepsilon = \varepsilon_0$; nonlinearity of the $\sigma - \varepsilon$ curve actually begins at $\varepsilon = 0.95\varepsilon_0$. The transition region significantly enhances the convergence rate of the global Newton iterations. Wang [31] provides additional details of this constitutive model.

Finite element solutions for the wide-plate specimens and for the fracture specimens are performed using $n = 10$, $E/\sigma_0 = 500$ and $\nu = 0.3$. Numerical results are normalized by σ_0 and the appropriate specimen dimension (minimum of the crack length, a , or the remaining ligament, b) to accommodate variations in the actual yield stress and specimen size. The $n = 10$ exponent provides a good approximation to the measured $\sigma - \varepsilon$ curves for Plate 13A, 13B over the temperature range -40°C to 35°C (at lower temperatures a definitive Luder's band develops). The yield stress varies approximately 3–5% over this temperature range.

4.2 Finite Element Models

Figure 7 shows the plane-strain finite element models defined for the wide-plate specimen, the SE(B) specimen with $a/W = 0.1$ and the C(T) specimen. Symmetry conditions permit modeling of only one-half of each specimen. A typical half-symmetric mesh contains 600 elements and 1600 nodes. Eight-noded isoparametric elements with reduced (2x2) Gauss quadrature are employed in all of the models. Reduced integration eliminates locking of arbitrarily shaped elements once the incompressible conditions of fully plastic deformation constrain volumetric changes in the displacement gradients.

Concentric rings of polygonal-shaped elements surround the crack tips. The innermost ring contains elements collapsed into wedge shapes with side nodes retained at the mid-point position. Initially coincident nodes at the crack tip are left unconstrained. This model produces a $1/r$ strain singularity appropriate for $n \rightarrow \infty$ and allows blunting deformations of the tip. The concentric rings of elements have sizes that increase geometrically with r . The mesh gradation provides at least 5–8 elements over the domain $1 < r/\delta_t < 5$, except for the very earliest stages of loading when δ_t is truly infinitesimal.

The organization and size of the central core of elements in the crack tip region is common for all meshes. The core elements are divided into 40 rings of increasing size with 10 elements per ring (6 in the forward sector). Elements incident on the crack tip have side length $W/L_e = 1400$ for a 1(T) specimen.

4.3 Solution Procedures

Loads are increased to final values in variably sized increments, typically a total of 40 increments, with full Newton iterations performed within each increment. Stringent criterion are specified to ensure convergence of strains and stresses in the third significant figure. Three to five iterations per increment are generally required for convergence. Given the strain path independence of stresses in deformation plasticity, converged values for strains and stresses are invariant of the load increment sizes used in the computations. The number and magnitude of the load increments is selected to provide a complete description of the response history and to maintain quadratic convergence of the Newton iterations.

J -integral values are obtained using the domain integral method [32,33]. The variation among J -values computed over element rings adjacent to the crack tip elements and rings remote from the tip is less than 1% as expected for the very refined models and deformation plasticity.

Numerical computations were performed on HP 9000 workstations using PATRAN [22] for mesh generation and Finite [9] for analyses and domain integral computations.

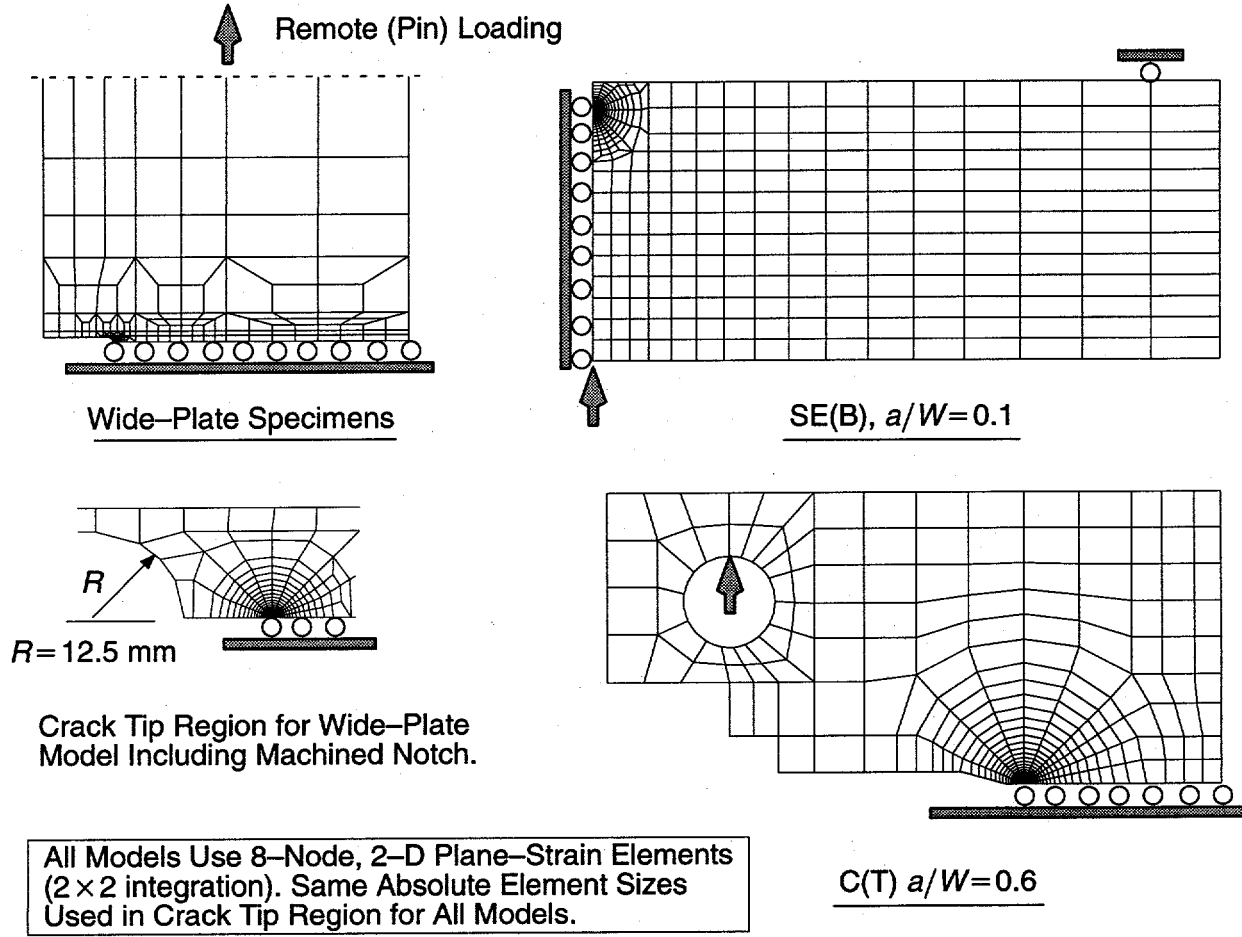


Figure 7. Finite element models for analyses of wide-plate and fracture test specimens.

4.4 Small-Scale Yielding Solutions

Figure 8 shows the opening mode stresses on the crack plane for the SSY ($T=0$) model obtained for this constitutive model using finite element analyses in a related study [14]. For convenience in post-processing finite element solutions of fracture test specimens, continuous functions are constructed to fit the SSY stresses which take the form

$$\frac{\sigma_{\theta\theta}}{\sigma_0} = \alpha \hat{r}^\beta \exp(\gamma \hat{r}) \quad (16)$$

where

$$\hat{r} = \frac{r}{J/\sigma_0 \epsilon_0} \quad (17)$$

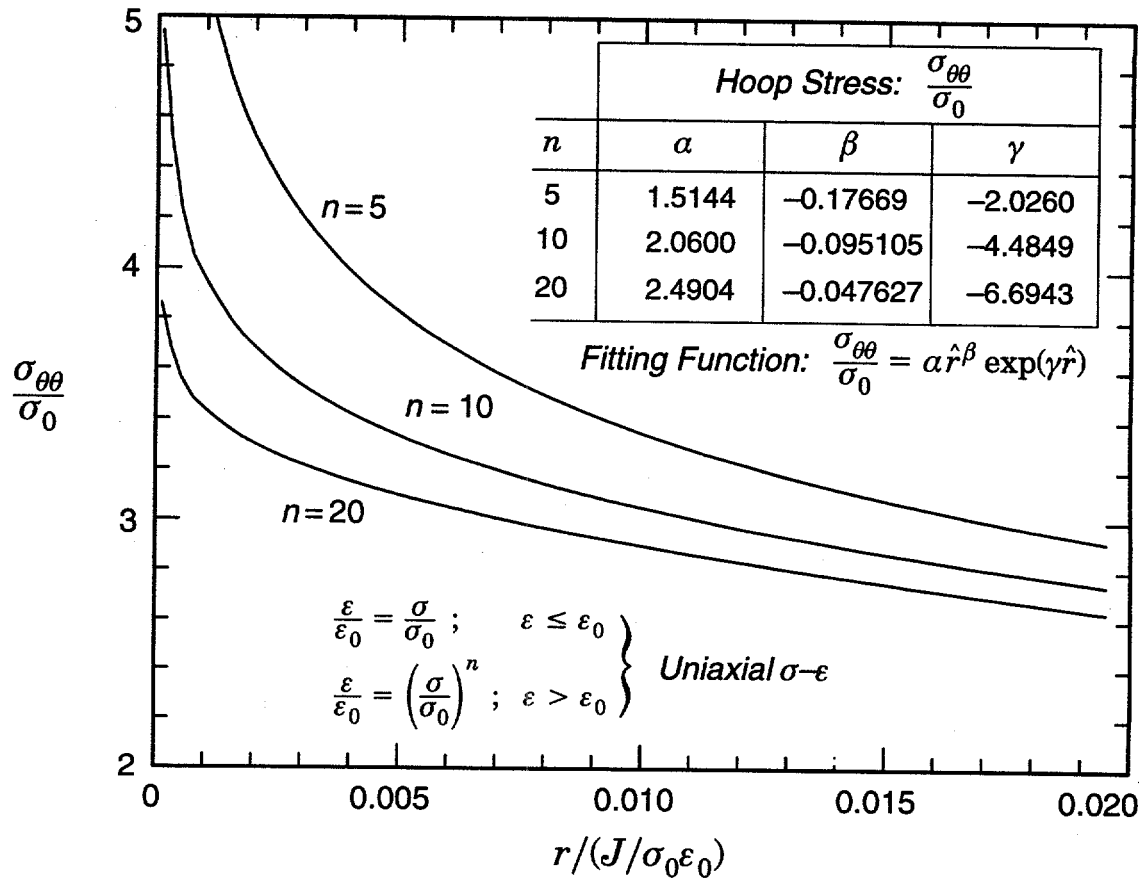


Figure 8. Opening mode stresses on crack plane for small-scale yielding ($T=0$). Uniaxial σ - ε model is power-law hardening after an initial linear response (small-strain analyses).

and α, β, γ are curve fitting parameters. The table included in Fig. 8 lists the values of these parameters for $n = 5, 10$ and 20 .

4.5 Effects of Side Grooves and Chevron Notching

The plane-strain finite element model for the wide-plate specimens includes the 25 mm wide by 187 mm long machined notch with a semi-circular tip at which the ~ 13 mm long sharp crack forms. However, this model cannot include directly the effects of side grooves present in all four specimens listed in Table 1 and the chevron notch present in specimens WP-1.3, 1.5 and 1.6. Post-test analyses conducted using a 3-D linear-elastic model (with side grooves and chevron notches) predicted K_I values larger at mid-thickness on the crack front relative to values obtained with the present plane-strain model at common values of remotely applied stress, σ^∞ (K_I values at fracture listed in Table 1 are predicted from the 3-D analyses).

The following procedure defines an approximate method to incorporate the effects of side grooves and chevron notches within the framework of the nonlinear plane-strain analyses performed here to study constraint effects on fracture initiation loads. Using the specimen dimensions, remote stresses at fracture and K_I values at fracture listed in Table 1, a non-dimensional geometry factor, F_{3-D} , is defined for each specimen by

$$F_{3-D} = \frac{K_I^{3-D}}{\sigma_{3-D}^{\infty} \sqrt{\pi a_0}} \quad . \quad (18)$$

where σ_{3-D}^{∞} denotes the experimentally measured (remote) stress at fracture in the wide-plate specimens. A linear-elastic analysis of the plane-strain, wide-plate model shown in Fig. 7 provides the plane-strain value of the geometry factor, $F_{2-D} = 1.365$, from

$$F_{2-D} = \frac{K_I^{2-D}}{\sigma_{2-D}^{\infty} \sqrt{\pi a_0}} \quad . \quad (19)$$

where the plane-strain value for K_I above is obtained from the domain integral J -value using the conversion defined by Eq (2). At fracture in each wide-plate test, simple estimates (neglecting the machined notch) indicate a plastic zone size on the order of 30 mm; consequently, the specimens remain essentially linear elastic with nonlinear stresses in the crack tip region loading governed by K_I and the T -stress. To approximate the 3-D effects, the plane-strain model is subjected to an increased, *effective* remote stress which makes $K_I^{2-D} = K_I^{3-D}$. Using Eqs (18,19), the effective stress is given by

$$\sigma_{eff}^{\infty} = \sigma_{3-D}^{\infty} \frac{F_{3-D}}{F_{2-D}} \quad . \quad (20)$$

Table 3 summarizes the effective stress at fracture for each of the wide-plate test specimens.

The nonlinear analysis of the plane-strain model for the wide-plate specimens provides the evolution of J and the constraint parameters (Q, J_0) with increasing levels of remotely applied stress. Estimates of J_c-Q and J_0 at fracture in each wide-plate specimen, shown in Table 3, are given by results of the plane-strain model evaluated at the effective value of remotely applied stress (20) listed in Table 3.

5. Results and Discussions

The wide-plate specimens experienced cleavage fracture initiating from the starter crack at temperatures ($T-RT_{NDT}$, °C) of -10, -28, -7 and +4 for specimens WP-1.2, 1.3, 1.5 and 1.6, respectively (refer to Table 1). Corresponding values of fracture toughness for the material are available at temperatures ($T-RT_{NDT}$, °C): -27, +5 for Plate 13A and for -25, -8, +8 for Plate 13B (refer to Figs. 2 and 3). In the analyses of constraint effects described subsequently, these results are treated in two groups. In group one, the measured response of specimen WP-1.3 is compared to material toughness data for Plate 13A at -27 and Plate 13B at -25 ($T-RT_{NDT}$, °C). In group two, the measured responses of specimens WP-1.2, 1.5, 1.6 are compared to material toughness data for Plate 13A at +5 and for Plate 13B at -8, +8 ($T-RT_{NDT}$, °C).

SE(B) specimens used to perform fracture toughness tests on Plate 13B material have the same thickness (~ 100 mm) as the wide-plate specimens. However, fracture tests performed on Plate 13A used 25 mm and 50 mm thick C(T) specimens providing a ratio of 4:1 and 2:1 in plate thickness relative the wide-plate specimens. Previous experimental and theoretical work [30,29] on ferritic steels in the transition region demonstrates an absolute thickness effect on fracture toughness not related to constraint. Metallurgical variations in the material along the crack front require a statistical treatment of thickness in experimental fracture toughness data. Wallin [30] employs weakest link statistics to obtain the following statistical correction for fracture toughness data in specimens of different thickness (B_1 and B_0) which fail by cleavage without previous ductile tearing,

$$K_{\text{corr},1} = K_{\text{min}} + (K_{Ic,0} - K_{\text{min}}) \left(\frac{B_0}{B_1} \right)^{1/4} \quad (21)$$

Recasting Eq (21) in terms of J yields,

$$J_{\text{corr},1} = J_{\text{min}} + (J_{c,0} - J_{\text{min}}) \left(\frac{B_0}{B_1} \right)^{1/2} \quad (22)$$

The corrections given in Eqs (21,22) arise solely from the different volume of material sampled along the crack front due to the different thicknesses. Each point along the crack front is *assumed* to be stressed at the same level. As the sampled volume increases, the probability of finding a metallurgical weak link increases. Because the failure of a weak metallurgical defect controls cleavage fracture, fracture toughness decreases with increasing probability of finding a defect. J_{min} for ferritic materials is quite small ($\sim 2-3 \text{ kJ/m}^2$) and can be neglected in the above equation.

Table 3. Effective stresses, J_c - Q and J_0 values at fracture for plane-strain models of WP-1 series test specimens.

Quantity	Specimen Designation			
	WP-1.2	WP-1.3	WP-1.5	WP-1.6
σ_{3-D}^{∞} exp. at fracture (MPa)	186	113	108.5	142.5
K_I^{3-D} at fracture (MPa $\cdot \sqrt{m}$)	252	174	180	232
Initial crack length (a_0 , mm)	199	197	200	200
F_{3-D} (Eq 18)	1.71	1.96	2.09	2.05
σ_{eff}^{∞} at fracture (Eq 20, MPa)	233	162.3	166.1	214
J_c (using σ_{eff}^{∞} , kJ/m^2)	309	141	148	255
Q (at fracture using J_c)	-0.33	-0.23	-0.25	-0.31
J_0 (at fracture using J_c , kJ/m^2)	131	78.3	83.3	120
J/J_0 (at fracture)	2.36	1.80	1.78	2.13
$F_{2-D} = 1.365$				

To apply this statistical thickness correction for the Plate 13A C(T) tests, the measured J_c -values for the 25 mm and 50 mm thicknesses are *corrected* to a 100 mm thickness by reducing (multiplying) the measured values by $(25/100)^{1/2} = 0.5$ and $(50/100)^{1/2} = 0.7$, respectively.

5.1 Constraint Assessment Using J - Q Theory

Figure 9 provides the J - Q driving force curves determined from the finite element analyses for the wide-plate model and for the various specimens used to obtain the fracture toughness values shown in Figs. 2 and 3 ($a/W = 0.1, 0.5$ SE(B)s and $a/W = 0.6$ C(T)s). With J normalized as shown by the crack length, a , (or remaining ligament, b) and yield stress, one curve for each configuration suffices to describe the results for different absolute specimen sizes having these material flow properties (linear plus power-law hardening, $n = 10$ and $E/\sigma_0 = 500$). Note that

E/σ_0 ratios for the A533B materials described in Table 2 are somewhat smaller than the nominal value of 500 used in the finite element analyses.

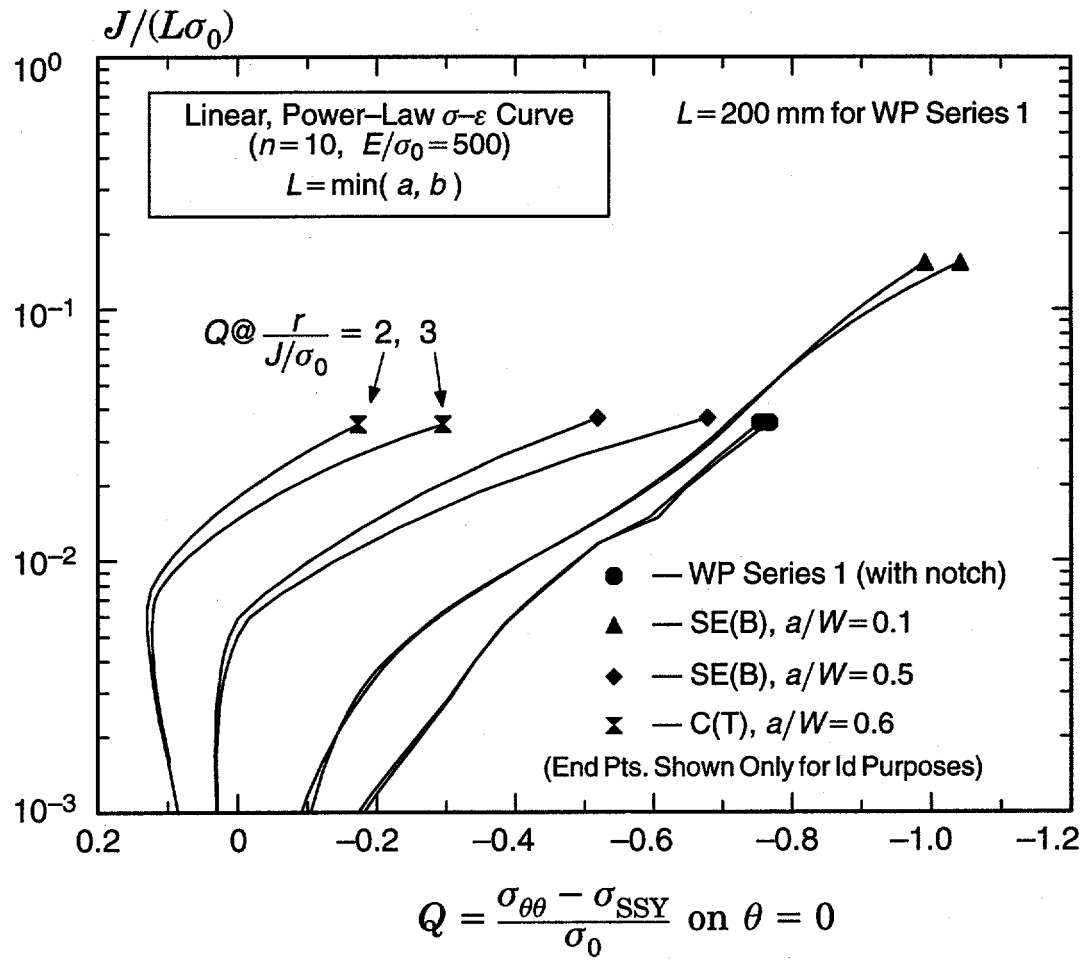


Figure 9. Normalized J - Q driving force curves for wide-plate specimens and fracture test specimens. Computed using plane-strain analyses; no size corrections are included.

While Fig. 9 using normalized J -values to scale specimen size effects on the J - Q driving force curves proves convenient to represent a large class of results, comparisons of actual J - Q values at fracture for a specific material-temperature combination requires unnormalized J -values reflecting the actual specimen sizes involved (e.g., an $a/W=0.1$ SE(B) can have more or less constraint than the WP depending on the actual specimen size; a sufficiently large (L) SE(B) specimen remains in SSY). Figure 10 shows such results for the A533B wide-plate material at a temperature of $T-RT_{NDT}=-25$ °C. The unnormalized J - Q driving force curves are obtained from Fig. 9 using nominal specimen sizes, a/W ratios (e.g., 0.10 rather than 0.11) and a uniform $\sigma_0 = 415$ MPa. J_c - Q pairs at fracture for the C(T) and SE(B) specimens indicated in Figs. 2 and 3 and for WP-1.3 (see Table 3) at this temperature are shown. The small variations in size, a/W ratio and yield stress among specimens leads to Q -values that do not coincide exactly with the "nominal" J - Q driving force curves indicated on the figure. Six SE(B) toughness values are available at this temperature but only 2, 1-T C(T) values are available; the C(T) values shown reflect the thickness correction of Eq (22). The test reports indicate ductile crack

extension prior to cleavage fracture of less than 0.1 mm for these specimens. The dashed line sketched on the figure suggests an upper limit of the toughness locus determined by this (limited) data set of SE(B) and C(T) results. The test result for wide-plate specimen WP-1.3 is entirely consistent with this upper limit.

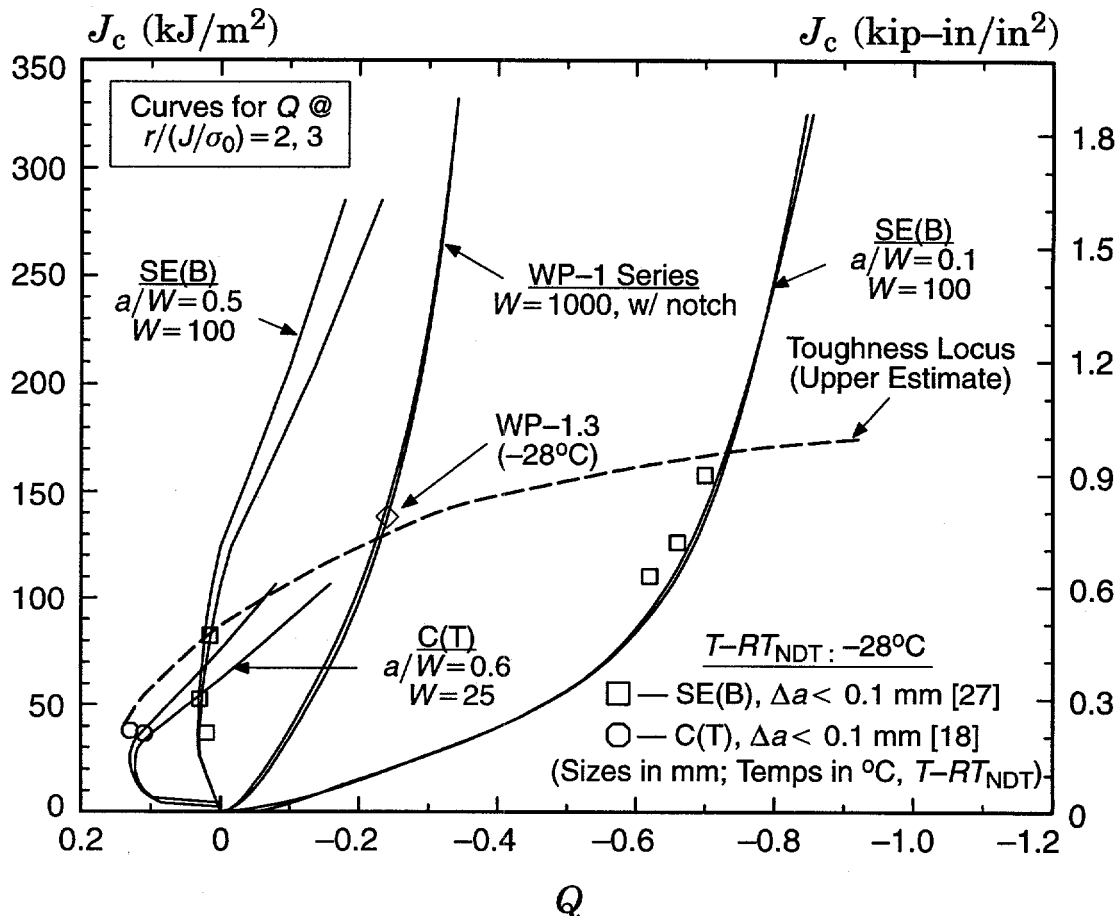


Figure 10. J - Q driving force curves and estimate of upper toughness locus for A533B material at -28°C . WP-1.3, SE(B) and C(T) fracture points are indicated.

Figure 11 shows a similar assessment for the three remaining wide-plate tests conducted at higher temperatures. Eight SE(B) and six C(T) fracture toughness values are available as shown on the figure for this temperature range. Specimens tested at the upper-end of the temperature range experienced ductile tearing of 0.4–0.8 mm prior to cleavage. Additional specimens experiencing more than 1 mm of prior ductile growth are not included in this assessment. The J - Q assessment neglects the potential impact of tearing on Q -values. Two dashed lines are sketched on the figure to suggest an upper and lower toughness locus determined by the data set of SE(B) and C(T) results. The lower curve defines a locus for no ductile tearing prior to cleavage; the higher curve reflects the larger J_c -values that develop with tearing. Not surprisingly, ductile tearing elevates significantly J_c -values in both the high and low constraint regions of the toughness locus. The WP-1.5 result appears in best agreement with the no ductile growth locus; it is at the low end of the temperature range (as is WP-1.2) and has the chevron notched crack front (WP-1.2 has no chevron notch).

In both assessments, the J - Q driving force curves at these loading levels reveal almost no dependence on distance ahead of the crack tip selected to evaluate Q for the wide-plate specimens and the shallow notch SE(B) specimens. However, the deep notch SE(B) and the C(T) specimens show a gradually increasing dependence of Q -values once the global bending deformation impinges strongly on the crack tip fields. The 1-T C(T) specimen maintains high constraint ($Q \sim +0.12$) at low loading but then loses constraint very rapidly under further loading. Despite the tension loading and small a/W ratio of the wide-plate specimens, their very large size enables the maintenance of constraint levels greater than the shallow notch SE(B)s of size $W=B=100$ mm.

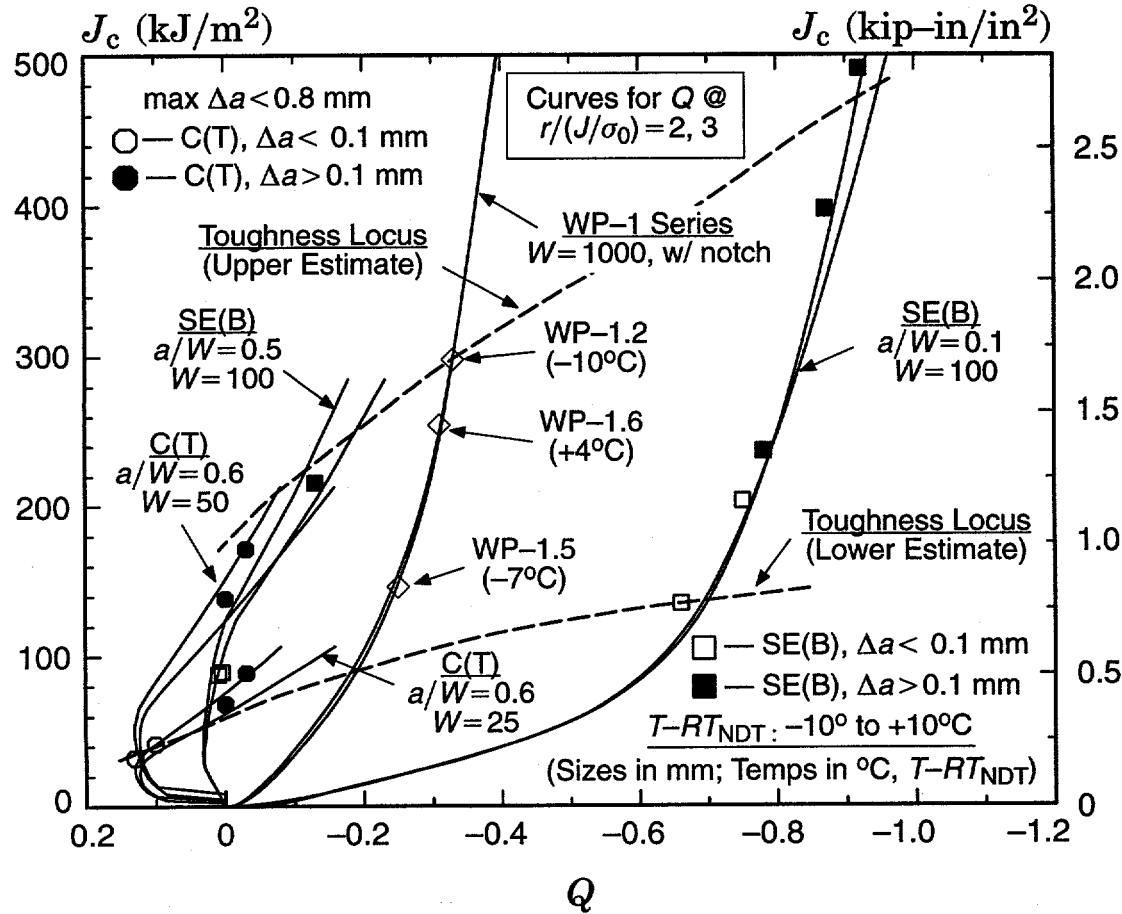


Figure 11. J - Q driving force curves and estimates of toughness locus for A533B material at -10°C to $+10^\circ\text{C}$ ($T-RT_{NDT}$). WP-1.2, 1.5, 1.6, SE(B) and C(T) fracture points are indicated.

5.2 Constraint Assessment Using Toughness Scaling

Figure 12 provides the toughness scaling models computed for the wide-plate specimen and for the various specimens used to obtain the fracture toughness values shown in Figs. 2 and 3 ($a/W=0.1, 0.5$ SE(B)s and $a/W=0.6$ C(T)s). These results are obtained by comparing the opening mode stresses on the crack plane in the fracture specimens (denoted FS) at distances of $r/(J_{FS}/\sigma_0) = 2, 3$ to those in SSY, rather than by using the more complex, contour area procedures outlined in Section 3.2. Dodds, et al. [11] discuss the agreement of J_0 values predicted using each of these two procedures. The crack-plane procedure is quite simple to apply. At each

loading level in the fracture specimen, the normalized value of opening mode stress, $\sigma_{\theta\theta}/\sigma_0$, at $\hat{r}_{FS} = r/(J_{FS}/\sigma_0) = 2$ is obtained from the finite element results. At the identical $\sigma_{\theta\theta}/\sigma_0$ in SSY, the normalized distance is found to be $\hat{r}_{SSY} = \beta \hat{r}_{FS}$ using the SSY stresses shown in Fig. 8 ($\beta > 1$ if the fracture specimen has less constraint than SSY). The ratio of J_{FS}/J_0 which generates the same opening mode stress at the same absolute distance ahead of the crack tip in each case (set $r_{SSY} = r_{FS}$) is then given simply by the ratio $\hat{r}_{SSY}/\hat{r}_{FS}$. By repeating this process at $\hat{r}_{FS} = 3$, for example, the effects on J_{FS}/J_0 of the global deformation field impinging on the crack tip fields may be examined (a similar comparison of Q at these distances is shown in Fig. 9).

The deep-notch bending specimens, SE(B) and C(T), exhibit the largest differences in J_{FS}/J_0 with \hat{r}_{FS} once the high constraint condition degenerates due to impingement of the bending field on the crack tip; the shallow-notch SE(B) and wide-plate specimens reveal much less sensitivity to \hat{r}_{FS} . These observations are fully consistent with those for the dependence of Q on distance from the crack tip illustrated in Fig. 9. At the maximum deformation shown for the wide-plate specimen ($J_{FS} = 3,350 \text{ kJ/m}^2$), only a 5% difference exists in the predicted J_0 values for $\hat{r}_{FS} = 2, 3$. For J -values at fracture in the wide-plate specimen ($J_{c-max} = 300 \text{ kJ/m}^2$), the difference falls below 1%.

Figure 13 shows the SSY (constraint corrected) toughness value, J_0 , for each corresponding fracture toughness value given in Figs. 2 and 3 (values at $T-RT_{NDT} < -30^\circ\text{C}$ are not needed).

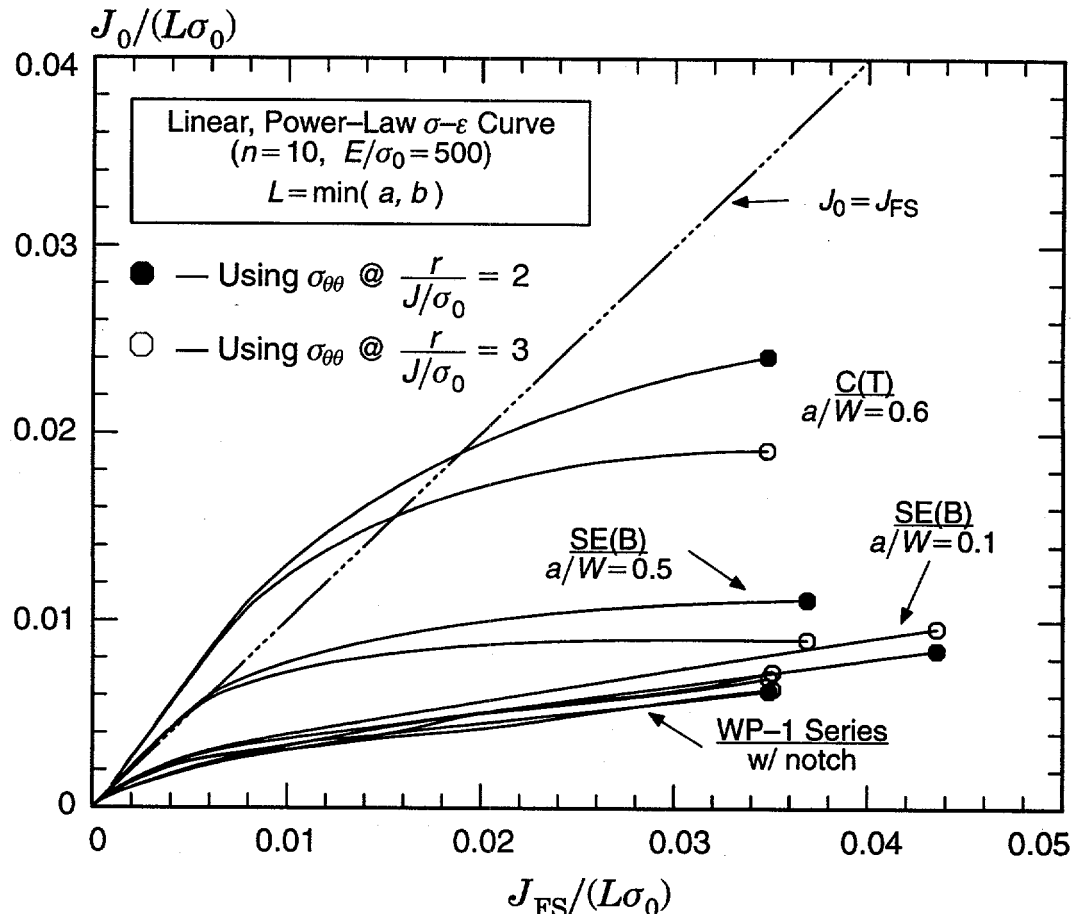


Figure 12. Normalized toughness scaling results for wide-plate specimens and fracture test specimens. (Scaling model curves constructed using opening mode stress on $\theta = 0$).

Specimens with a reported ductile crack growth > 0.1 mm prior to fracture are indicated by solid symbols. For the C(T) specimens, J_c values shown in Fig. 2 are constraint corrected to J_0 values and then the J_0 values are statistically corrected to a 100 mm thickness using Eq (22). Both the uncorrected J_c value (see Table 3) and corrected J_0 value for each wide-plate specimen are indicated on this figure. Fracture toughness values for the C(T) specimens and the $a/W = 0.5$ SE(B) specimens received negligible constraint corrections; for most C(T) specimens J_0 is greater than J_c due to the very high constraint present at fracture. The statistical thickness correction for the C(T) specimens to the same 100 mm thickness of the SE(B) specimens plays a dominant role in this assessment (J_0 values are reduced by factors of 0.5 and 0.71 for the 1-T and 2-T specimens, respectively). Tables in Appendix A summarize data for the C(T) and SE(B) fracture test specimens.

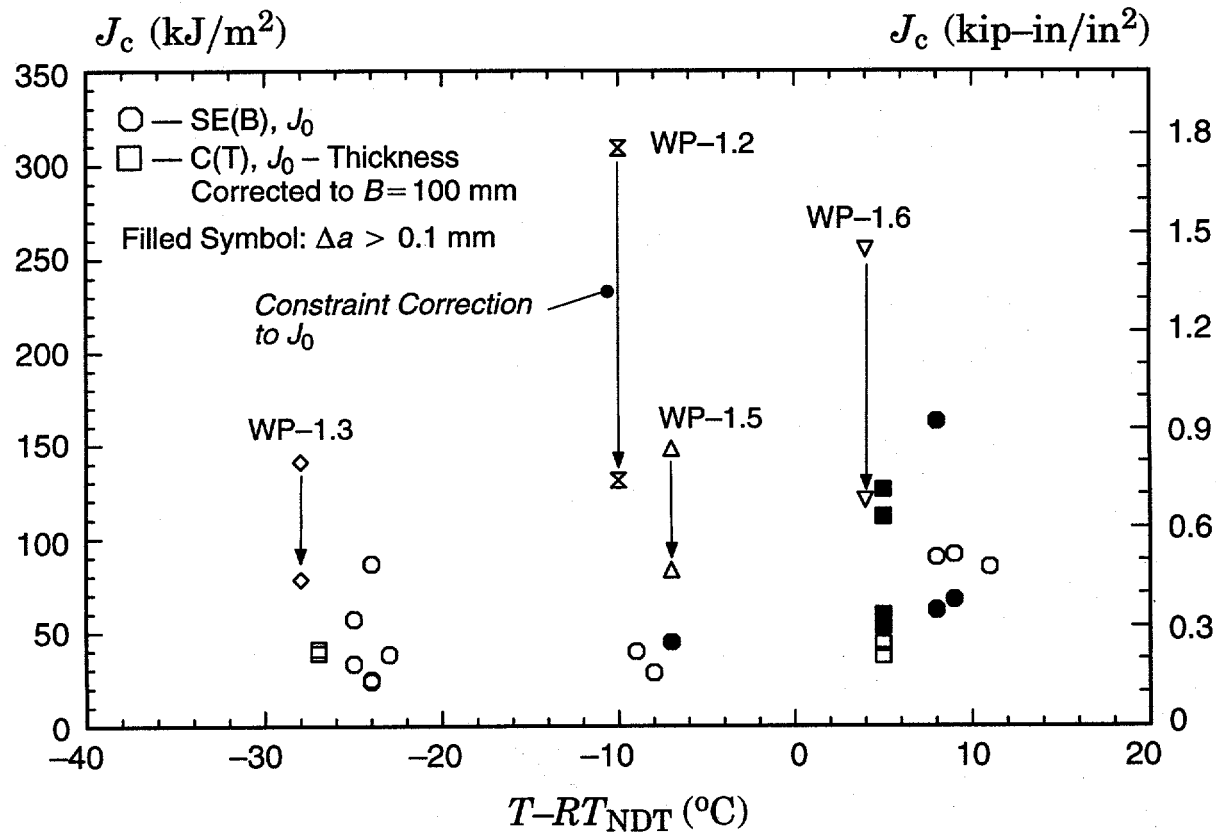


Figure 13. Constraint corrected toughness values (J_0) for wide-plate specimens and SE(B), C(T) test specimens.

J_0 values for WP-1.3 and WP-1.6 fall at the upper end of the scatter found in fracture toughness values at corresponding $T - RT_{NDT}$ values of -28 and $+8$ $^{\circ}\text{C}$. With only 3 fracture toughness values available at -8 $^{\circ}\text{C}$, the comparisons for WP-1.2 and WP-1.5 are less meaningful. However, it can be argued that additional toughness tests at -8 $^{\circ}\text{C}$ would predict values equal to or greater than those measured at -28 $^{\circ}\text{C}$. Constraint corrected toughness values for WP-1.2 and WP-1.5 would then lie at the upper-end of the scatter at -8 $^{\circ}\text{C}$.

The seemingly large J_{FS}/J_0 ratios for the wide-plate specimens arise from two interacting features of this geometry: (1) the inherent negative T -stress in this SE(T) geometry and (2) the proximity of the sharp crack tip to the rounded end of the 25 mm wide machined notch. The

$a/W=0.2$ SE(T) geometry of the wide-plate specimens generates a negative T -stress under loading which reduces the level of stress triaxiality at the crack tip when elastic-plastic conditions develop. For a simple $a/W=0.2$ SE(T) configuration, the geometry factor is $\beta = T\sqrt{\pi a}/K_I = -0.415$ [14,25]. Using the wide-plate results for specimen WP-1.2 as an example, the T -stress at fracture is $T/\sigma_0 = -0.29$ (using $K_I = 252$ from Table 3 and σ_0 from Table 2) which reduces the opening mode stress 9% below the SSY($T=0$) value. This degree of stress reduction exerts a strong effect on the J_{FS}/J_0 ratio. To demonstrate this, consider Figs. 14 and 15 which compare an $a/W=0.2$ SE(T) configuration without the notch to the wide-plate configuration (with the machined notch). The machined notch has the effect of making Q more negative and of increasing the J_{FS}/J_0 ratio over the range of J values at fracture in the wide-plate specimens. At much higher levels of plastic deformation, the notch has no effect (the distance $r = (2, 3)J/\sigma_0$ is much greater from the notch tip). Again using WP-1.2 as the example, $J_{FS}/J_0 = 1.82$ for the SE(T) without the notch (only the T -stress effect) while the ratio increases to 2.35 including the notch. In these wide-plate specimens, the inherent effect of the negative T -stress on elastic-plastic constraint is magnified significantly by the proximity of the large, traction-free notch tip (diameter of 25 mm compared to the actual sharp crack length of only 13 mm).

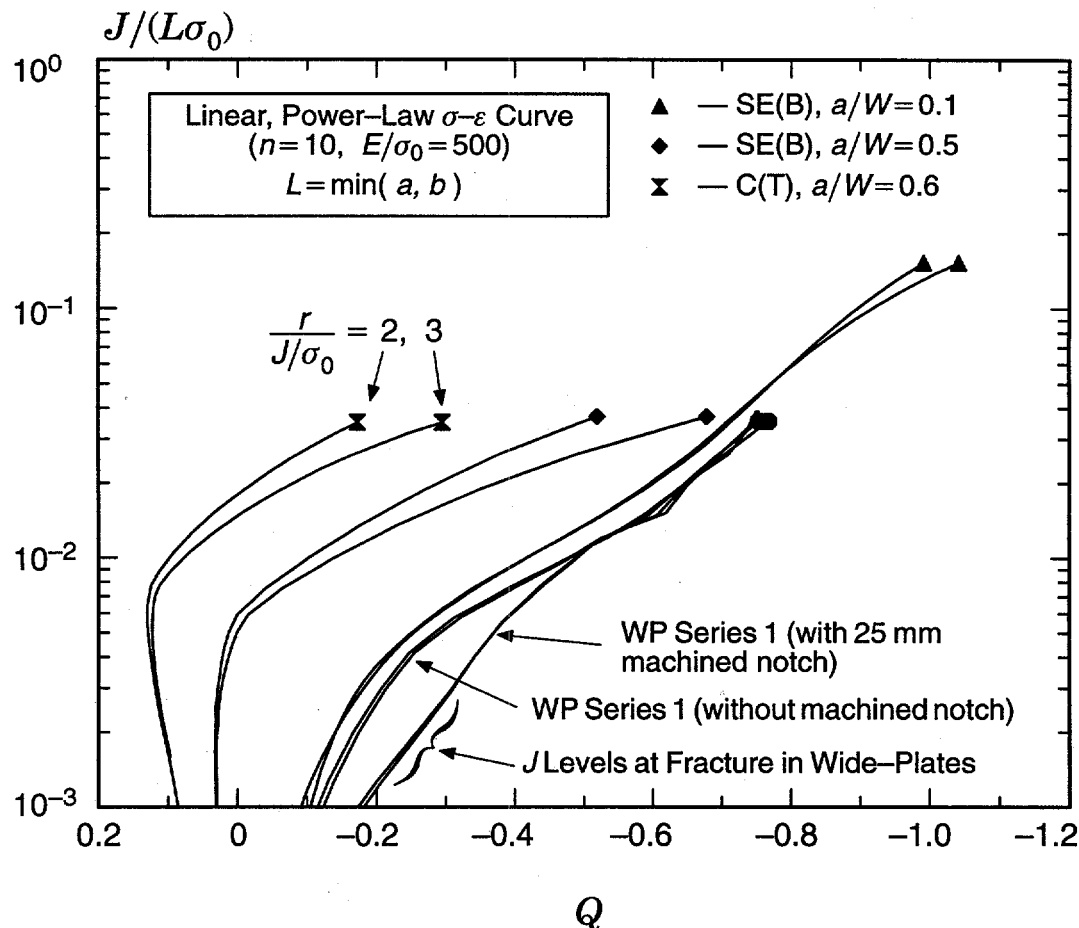


Figure 14. Effects of machined notch in wide-plate specimens on J - Q driving force curves.

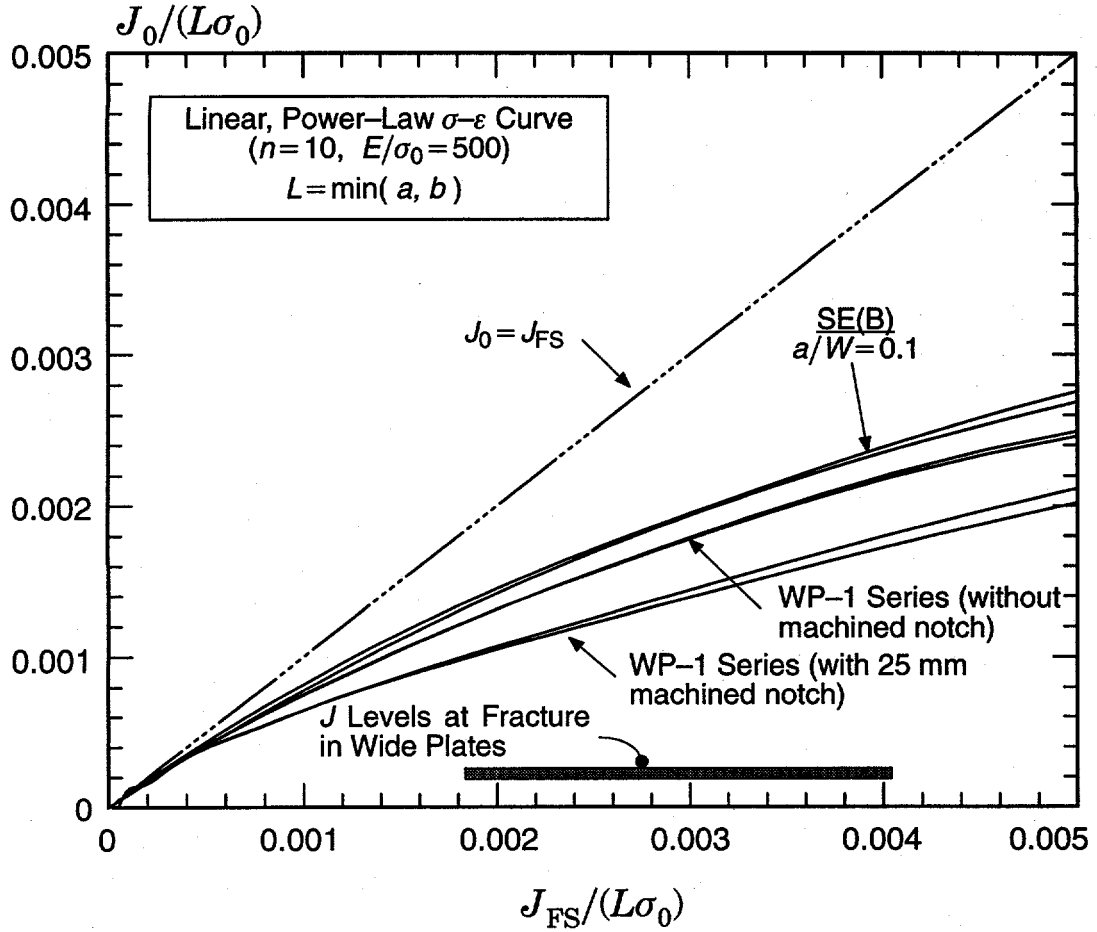


Figure 15. Effects of machined notch in wide-plate specimens on constraint scaling model to estimate J_0 .

The effects of ductile crack growth prior to cleavage fracture on J_0 values for the test specimens remains an issue. Recent work by Dodds et al. [26] examined the effects of small amounts of crack growth on the crack tip stresses driving the cleavage mechanism. For configurations exhibiting low constraint at J_{Ic} , e.g. SE(B)s with $a/W = 0.1$, subsequent increases in J_0 can equal increases J_{FS} after J_{Ic} for materials with low-to-moderate strain hardening and tearing modulus. During ductile growth, the near-tip stresses increase to levels approaching SSY primarily due to resharpening of the crack tip such that $\Delta J_0 \approx \Delta J_{FS}$. Moreover, crack extension subjects additional volumes of material to high stress, $\Delta V \approx \Delta a \times B$. For high constraint geometries, e.g., the C(T) and SE(B) with $a/W = 0.5$ here, the effects of growth are much less significant on J_0 values — crack growth has little effect on stress fields of a high constraint condition. The small data sets here preclude a quantitative treatment of tearing effects using the method proposed by Dodds et al [26]. However, their work demonstrates that J_0 values for the shallow notch SE(B) specimens in Fig. 13 with prior ductile extension are significantly “over-corrected” (J_0 values shown are too small).

6. Summary and Conclusions

The unexpectedly large fracture initiation loads for the A533B wide-plate specimens previously tested as part of the ORNL-HSST program are re-evaluated using two current methodolo-

gies to assess constraint effects on cleavage fracture: the two-parameter, $J-Q$, approach and the toughness scaling approach. The wide-plate specimens are nominally SE(T) configurations with $a/W = 0.2$ ($W = 1000$ mm, $B = 100$ mm) subjected to remote tension loading. Following an overview of the wide-plate test program and the two constraint assessment methodologies, plane-strain finite element analyses are described for the wide-plate configuration which include modifications to approximate the increased near-tip loading caused by side grooves and by crack-front chevron notches.

Finite element analyses are also described for SE(B) and C(T) fracture specimens which were used in the wide-plate test program to characterize the plate material. The finite element analyses provide the $J-Q$ driving force curves and the J/J_0 ratios needed to perform the constraint assessments. Fracture toughness tests are available for the Plate 13A material used to fabricate the wide-plate specimens and for a companion Plate 13B material. Compact specimens, 1-T and 2-T with $a/W = 0.6$, were used to test Plate 13A material while 4T SE(B) specimens with $a/W = 0.1, 0.5$ were used to test Plate 13B material. The fracture toughness values from these characterization studies provide data to construct $J-Q$ toughness loci for the material and to construct size independent estimates for the material toughness, J_0 , using the toughness scaling model.

The re-evaluation of wide-plate and fracture test specimen test results described here support the following observations and conclusions:

1. The computed $J-Q$ driving force curve for the wide-plate specimens indicates greater crack tip constraint than in SE(B) fracture specimens ($a/W = 0.1$ and $W = B = 100$ mm) but much less constraint than in the specimens tested for material characterization studies, $a/W = 0.5$ SE(B)s and $a/W = 0.6$ C(T)s. Over the range of J values at which fracture occurs in the wide-plate and the SE(B), C(T) specimens, Q values exhibit no significant dependence on the distance, $r/(J/\sigma_0)$, ahead of the crack tip selected to make the computation.
2. The SE(B) and C(T) fracture toughness tests enable construction of a $J-Q$ fracture toughness locus at -28 ($T-RT_{NDT}$, $^{\circ}\text{C}$) and for the range -8 to $+8$ ($T-RT_{NDT}$, $^{\circ}\text{C}$). The toughness locus for the higher temperature range exhibits considerable scatter, caused primarily by specimens that experience ductile crack growth prior to fracture (0.1 mm $< \Delta a < 1$ mm). $J-Q$ fracture locations for the wide-plate specimens lie at the upper-end of these toughness loci.
3. The computed relationships between conventional J values and the constraint corrected J_0 values for the wide-plate specimen and for the fracture specimens are fully consistent with the $J-Q$ driving force curves. Over the range of J values at which fracture occurs in the wide-plate and the SE(B), C(T) specimens, the corresponding J_0 values show no significant dependence ($< 5\%$) on distance, $r/(J/\sigma_0)$, ahead of the crack tip adopted for the computation.
4. Fracture toughness values measured for the deep-notch SE(B) and C(T) specimens require no constraint correction. Some shallow notch SE(B) results have J_c/J_0 ratios exceeding 4.0, i.e., those with ductile tearing prior to cleavage. Wide-plate J_c/J_0 ratios are WP-1.2 (2.4), WP-1.3 (1.8), WP-1.5 (1.8) and WP-1.6 (2.1). J_0 values for wide-plate specimens WP-1.3 (-28 $^{\circ}\text{C}$, $T-RT_{NDT}$) and WP-1.6 ($+4$ $^{\circ}\text{C}$, $T-RT_{NDT}$) lie within the scatter of corrected fracture toughness values available at those temperatures. Only three fracture toughness values are available for comparison with wide-plate specimens WP-1.2 and WP-1.5 (-10 $^{\circ}\text{C}$, $T-RT_{NDT}$). Consequently, the comparison for these two wide-plate specimens remains inconclusive, although the results are consistent with the trend of toughness values between those at -28 $^{\circ}\text{C}$ and $+8$ $^{\circ}\text{C}$ ($T-RT_{NDT}$).

5. The seemingly large J_c/J_0 ratios for the wide-plate specimens arise from two features: (a) the inherent negative T -stress for an $a/W = 0.2$ SE(T) geometry, $\beta = T\sqrt{\pi a}/K_I = -0.415$, lowers markedly the stress triaxiality in the near-tip stresses even under well-contained plasticity; and (b) the rounded tip of the 25 mm wide machined notch provides a relatively large, nearby traction free surface adjacent to the sharp crack which further lowers constraint. For example, the presence of the notch increases the J_c/J_0 ratio from 1.8 to 2.4 for specimen WP-1.2.
6. The statistical thickness correction for cleavage fracture in the transition region proposed by Wallin seems "consistent" within the framework of the toughness scaling model. J_c values are first "constraint" corrected to J_0 values and then "thickness" corrected to a convenient reference thickness ($B = 100$ mm in the present study). However, a similar "consistent" approach does not exist for the J - Q methodology. Q values here are derived from thickness corrected J_c values. The thickness correction is needed for the 1-T and 2-T C(T) toughness values to bring them to the same 100 mm thickness of the SE(B) and wide-plate specimens. The correction multipliers are 0.5 (1-T) and 0.71 (2-T).

7. References

1. Anderson, T.L., and Stienstra, D., "A Model to Predict the Sources and Magnitude of Scatter in Toughness Data in the Transition Region," *Journal of Testing and Evaluation*, Vol. 17, pp. 46-53, 1989.†
2. Anderson, T.L., and Dodds, R.H., "Specimen Size Requirements for Fracture Toughness Testing in the Ductile-Brittle Transition Region," *Journal of Testing and Evaluation*, Vol. 19, pp. 123-134, 1991.†
3. ASTM E399-83, "Standard Test Method for Plane-Strain Fracture Toughness of Metallic Materials," American Society for Testing and Materials, Philadelphia, Pennsylvania, 1983.†
4. Bass, B., et al., Martin Marietta Energy Systems, Inc., Oak Ridge Natl. Lab., "Biaxial Loading and Shallow-Flaw Effects on Crack Tip Constraint and Fracture Toughness," USNRC Report NUREG/CR-6132 (ORNL/TM-12498), January 1994.*
5. Beremin F. M., "A Local Criterion for Cleavage Fracture of a Nuclear Pressure Vessel Steel", *Metalurgical Transactions A*, V14A, pp. 2277-2287, 1983.†
6. Betegon, C., and Hancock, J.W., "Two-Parameter Characterization of Elastic-Plastic Crack Tip Fields," *Journal of Applied Mechanics*, Vol. 58, pp. 104-113, March 1991.†
7. Bilby, B.A., Cardew, G.E., Goldthorpe, M.R. and Howard, I.C., "Size Effects in Fracture," *Institution of Mechanical Engineers*, London, England, pp. 36-46, 1986.†
8. Bruckner, A. and Munz, D., "Prediction of Failure Probabilities for Cleavage Fracture From The Scatter of Crack Geometry and of Fracture Toughness Using the Weakest Link Model", *Engineering Fracture Mechanics*, V18, N2, pp. 359-375, 1983.†
9. Dodds, R.H., and Lopez, L.A., "Software Virtual Machines for Development of Finite-Element Systems," *International Journal for Engineering with Computers*, Vol. 13, pp. 18-26, 1985.†
10. Dodds, R.H., Anderson, T.L., and Kirk, M.T., "A Framework to Correlate a/W Ratio Effects on Elastic-Plastic Fracture Toughness (J_c)," *International Journal of Fracture*, Vol. 48, pp. 1-22, 1991.†
11. Dodds, R.H., Shih, C.F., and Anderson, T.L., "Continuum and Micromechanics Treatment of Constraint in Fracture," *International Journal of Fracture*, Vol. 64, pp. 101-133, 1993.†
12. Du, Z.Z., and Hancock, J.W., "The Effect of Non-Singular Stresses on Crack Tip Constraint," *Journal of the Mechanics and Physics of Solids*, Vol. 39, pp. 555-567, 1991.†
13. Faleskog, J. and Nordlund, P., "Near-Tip Field Characterization and J -Integral Evaluation for Nonproportional Loads," *International Journal of Solids & Structures*, Vol. 31, pp. 1-26, 1994.†
14. Kirk, M.T., and Dodds, R.H., "Approximate Techniques for Prediction of Size Effects on Cleavage Fracture Toughness," *ASTM STP1207*, J. Landes, D. McCabe and Boulet, Eds., American Society for Testing and Materials, Philadelphia, 1994.†

15. Koers, R. W. J., Krom, A. H.M., and Bakker, A., "Prediction of Cleavage Fracture in the Brittle to Ductile Transition Region of a Ferritic Steel," *Constraint Effects in Fracture: Theory and Applications, ASTM STP1224*, Mark Kirk and Ad Bakker Eds., American Society for Testing and Materials, Philadelphia, 1994.†
16. Larsson, S.G., and Carlsson, A.J., "Influence of Non-Singular Stress Terms and Specimen Geometry on Small-Scale Yielding at Crack Tips in Elastic-Plastic Materials," *Journal of the Mechanics and Physics of Solids*, Vol. 21, pp. 263-277, 1973.†
17. Leevers, P.C. and Radon, J.C., "Inherent Stress Biaxiality in Various Specimen Geometries," *International Journal of Fracture*, Vol. 19, pp. 311-325, 1982.†
18. Naus, D. J. et al., Martin Marietta Energy Systems, Inc., Oak Ridge Natl. Lab., "Crack-Arrest Behavior in SEN Wide Plates of Quenched and Tempered A533 Grade B Steel Tested Under Nonisothermal Conditions," USNRC Report NUREG/CR-4930 (ORNL/TM-6388), August 1987.*
19. O'Dowd, N.P., and Shih, C.F., "Family of Crack Tip Fields Characterized by a Triaxiality Parameter: Part I - Structure of Fields," *Journal of the Mechanics and Physics of Solids*, Vol. 39., No. 8, pp. 989-1015, 1991.†
20. O'Dowd, N.P., and Shih, C.F., "Family of Crack Tip Fields Characterized by a Triaxiality Parameter: Part II - Fracture Applications," *Journal of the Mechanics and Physics of Solids*, Vol. 40, pp. 939-963, 1992.†
21. Parks, D.M., "Advances in Characterization of Elastic-Plastic Crack Tip Fields," *Topics in Fracture and Fatigue*, Ed. A.S. Argon, Springer-Verlag, pp. 59-98, 1992.†
22. PATRAN User's Manual, Release 2.5, PDA Engineering Inc., Costa Mesa, California, 1993.§
23. Rice, J.R., "A Path Independent Integral and the Approximate Analysis of Strain Concentration by Notches and Cracks," *Journal of Applied Mechanics*, Vol. 35, pp. 379-386, 1968.†
24. Ritchie, R. O., Knott J. F. and Rice, J. R., "On the relationship Between Critical Tensile Stress and fracture Toughness in Mild Steel", *J. Mech. Phys. Solids*, V21, pp. 395-410, 1973.†
25. Sham, T.L., "The Determination of the Elastic T -term using Higher Order Weight Functions," *International Journal of Fracture*, Vol. 48, pp. 81-102, 1991.†
26. Tang, M., Dodds, R.H. and Anderson, T.L., "Effects of Ductile Crack Growth on Constraint Models for Cleavage Fracture," *SRS 585, UILU-ENG-94-2001*, Department of Civil Engineering, University of Illinois at Urbana-Champaign, January 1994.*
27. Theiss, T. Shum, D. and Rolfe, S. Martin Marietta Energy Systems, Inc., Oak Ridge Natl. Lab., "Experimental and Analytical Investigation of the Shallow-Flaw Effect in Reactor Pressure Vessels," USNRC Report NUREG/CR-5886 (ORNL/TM-12115), July 1992.*
28. Wallin, K., Saario, T., and Torronen, K., "Statistical Model for Carbide Induced Brittle Fracture in Steel," *Metal Science*, Vol. 18, pp. 13-16, 1984.†
29. Wallin, K., "The Effect of Ligament Size on Cleavage Fracture Toughness," *Engineering Fracture Mechanics*, Vol. 32, 1989, pp. 449-457.†
30. Wallin, K., "Statistical Aspects of Constraint with Emphasis on Testing and Analysis of Laboratory Specimens in the Transition Region," *Constraint Effects in Fracture, ASTM STP 1171*, E.M. Hackett, K.H. Schwalbe, and R.H. Dodds, Eds., American Society for Testing and Materials, Philadelphia, pp. 264-288, 1993.†
31. Wang, Y.Y., "On the Two-Parameter Characterization of Elastic-Plastic Crack-Front Fields in Surface-Cracked Plates," *Constraint Effects in Fracture, ASTM STP 1171*, E.M. Hackett, K.H. Schwalbe, and R.H. Dodds, Eds., American Society for Testing and Materials, Philadelphia, pp. 2120-138, 1993.†
32. Williams, M.L., *Journal of Applied Mechanics*, Vol. 24, pp. 109-114, 1957.†

* Available for purchase from national Technical Information Service, Springfield, VA 22161.

† Available from public technical libraries.

‡ Copies are available from U.S. Government Printing Office, Washington, D.C. 20402. ATTN: Regulatory Guide Account.

§ Available for purchase from vendor.

Appendix A – Fracture Specimen Results and Constraint Assessment Values

Table A.1 Fracture Test Data for A533B Plate 13A C(T) Specimens.

Specimen	$T-RT_{NDT}$ (°C)	B (mm)	a_0/W	Δa (mm)	J_c (kJ/m ²)	J_c-100 (kJ/m ²)	Q	J_0 (kJ/m ²)	J_0-100 (kJ/m ²)
K54C	-27	25	0.566	0.05	76	38	0.130	82	41
K53B	-27	25	0.574	0.05	73	37	0.110	78	39
K53F	5	25	0.572	0.06	65	32	0.130	76	38
K54E	5	25	0.567	0.07	83	42	0.100	88	44
K51D	5	25	0.570	0.16	136	68	0.000	106	53
K53E	5	25	0.562	0.20	178	89	-0.030	118	59
K41B	5	51	0.563	0.22	196	137	0.000	159	112
K34B	5	51	0.562	0.37	243	170	-0.028	179	126
K54F	5	25	0.568	1.12	124	62	—	—	—
K51A	5	25	0.573	1.05	501	251	—	—	—

Notes:

1. $RT_{NDT} = -23^{\circ}\text{C}$
2. J_c = reported J at cleavage fracture
3. $J_c-100 = J_c$ corrected to $B = 100$ mm using Eq (22)
4. Q is based on J_c-100
5. J_0 = constraint corrected J_c value
6. $J_0-100 = J_0$ corrected to $B = 100$ mm using Eq (22)
7. Specimens were *not* side-grooved
8. Specimens K54F and K51A had more than 1 mm crack growth and are not considered

Table A.2 Fracture Test Data for A533B Plate 13B SE(B) Specimens.

HSST Beam No.	T-RT _{NDT} (°C)	a_0/W	Δa (mm)	J_c (kJ/m ²)	Q	J_0 (kJ/m ²)
28	9	0.10	0.750	491	-0.92	68
18	-9	0.10	—	204	-0.75	40
27	-7	0.11	0.270	237	-0.78	45
21	-8	0.11	—	135	-0.66	29
38	-24	0.11	0.074	111	-0.62	24
37	-24	0.11	—	126	-0.66	25
20	11	0.11	—	686	-1.08	89
22	8	0.11	0.540	398	-0.87	62
26	-25	0.11	—	158	-0.70	33
31	-25	0.51	0.011	53	0.03	57
36	-23	0.51	—	37	0.02	38
35	8	0.51	—	88	0.01	90
25	-24	0.51	—	82	0.01	87
24	8	0.51	0.342	216	-0.13	163
17	9	0.52	—	90	0.01	92

Notes:

1. $RT_{NDT} = -15^\circ\text{C}$
2. All specimens are SE(B) with $W = B = 100$ mm
3. J_c = reported J at cleavage fracture
4. J_0 = constraint corrected J_c value
5. Specimens were *not* side-grooved
6. Specimens at lower temperatures omitted
7. Crack growth measurements available only for 6 specimens indicated above

Internal Distribution

1. D. J. Alexander	16. D. E. McCabe
2-5. B. R. Bass	17. J. G. Merkle
6. J. W. Bryson	18. R. K. Nanstad
7. W. R. Corwin	19-23. W. E. Pennell
8. T. L. Dickson	24. C. E. Pugh
9-10. R. G. Gilliland	25. M. C. Rao
11. F. M. Haggag	26. ORNL Patent Section
12. W. F. Jackson	27. Central Research Library
13. S. K. Iskander	28. Document Reference Section
14. J. A. Keeney	29-30. Laboratory Records
15. W.J. McAfee	31. Laboratory Records(RC)

External Distribution

32. J. W. Craig, Deputy Director, Division of Engineering, RES, U.S. Nuclear Regulatory Commission, Washington, DC 20555-0001
33. K. R. Wichman, Division of Engineering, NRR, U.S. Nuclear Regulatory Commission, Washington, DC 20555-0001
34. L. C. Shao, Director, Division of Engineering, RES, U.S. Nuclear Regulatory Commission, Washington, DC 20555-0001
35. T. P. Speis, Deputy Director, Office of Nuclear Regulatory Research, U.S. Nuclear Regulatory Commission, Washington, DC 20555-0001
- 36-38. S. N. M. Malik, Division of Engineering, U.S. Nuclear Regulatory Commission, Washington, DC 20555-0001
39. M. E. Mayfield, Division of Engineering, U.S. Nuclear Regulatory Commission, Washington, DC 20555-0001
40. G. R. Irwin, Department of Mechanical Engineering, University of Maryland, College Park, MD 20742
41. C. F. Shih, Box D, Division of Engineering, Brown University, Providence, RI 02912
- 42-46. R. Dodds, 3140 Newmark Laboratory, 205 North Matthews, Urbana, IL 61801
47. R. Fields, National Institute of Standards and Technology, Bldg. 223, B144, Gaithersburg, MD 20899
48. W. L. Fourney, Department of Mechanical Engineering, University of Maryland, College Park, MD 20742
49. S. T. Rolfe, The University of Kansas, Lawrence, KS 66045-2235
50. C. W. Schwartz, Department of Civil Engineering, University of Maryland, College Park, MD 20742
51. Office of Assistant Manager for Energy Research and Development, DOE-ORO, Oak Ridge, TN 37831
- 52-53. Office of Scientific and Technical Information, P.O. Box 62, Oak Ridge, TN 37831
54. Y. J. Chao, Mechanical Engineering, The University of South Carolina, Columbia Campus, Columbia, SC 29208
55. T. L. Anderson, Department of Mechanical Engineering, Texas A&M University, College Station, TX 77843
56. J. M. Joyce, U.S. Naval Academy, Annapolis, MD 21402